Contents lists available at ScienceDirect

Materials Science & Engineering A

Phase transformations during partitioning in a Q&P steel with blocky retained austenite

R. Mishnev [a,b,*], Yu. Borisova [a,b], T. Kniaziuk [a,c], R. Kaibyshev [a]

[a] Laboratory of Advanced Steels for Agricultural Machinery, Russian State Agrarian University–Moscow Timiryazev Agricultural Academy, 127550, Moscow, Russia
[b] Laboratory of Mechanical Properties of Nanostructured Materials and Superalloys, Belgorod State National Research University, 308015, Belgorod, Russia
[c] National Research Center "Kurchatov Institute"–Central Research Institute of Structural Materials "Prometey", 191015, St.-Petersburg, Russia

ARTICLE INFO

ABSTRACT

Effect of partitioning on structure and mechanical properties of a Fe-0.44%C-1.8%Si-1.3%Mn-0.82%Cr-0.28%Mo steel processed by quenching-partitioning (Q&P) was considered. This Q&P steel exhibited a superior combination of the yield stress (YS) of ~1150 MPa, ultimate tensile strength (UTS) of ~1650 MPa and elongation-to-failure (δ) of ~21 %. The product of strength and elongation (PSE – UTS $\times$ δ) was >30 GPa $\times$ % after partitioning, with a duration ranging from 60 to 500 s. During partitioning, three main processes occurred: the carbon partitioning between retained austenite (RA) and martensite/bainitic ferrite (BF), the transformation of blocky RA into bainite, and the precipitation of transition η–Fe_2C carbides in the martensitic matrix. The enrichment of RA by carbon changed the mechanism of bainitic transformation and then suppressed the formation of BF and induced the reverse growth of RA upon 500 s partitioning. The rate of carbon partitioning depends on the diffusion path that produces a wide distribution of carbon concentration in areas of RA. The formation of secondary martensite and bainite takes place in areas of untransformed austenite with relatively low carbon content. The effect of RA volume fraction on ductility and the PSE is insignificant. Carbon enrichment of RA ceased its transformation into strain-induced martensite and induced twinning during tension.

1. Introduction

Advanced high-strength steels (AHSS) are widely used by the automotive industry due to the attractive combination of high ultimate tensile strength (UTS) and ductility, δ, characterized by the product of strength and elongation (PSE = UTS $\times$ δ) (MPa $\times$ %) [1]. The third generation AHSS has to be both strong and ductile and exhibit a superior combination of high yield stress (YS) $\geq$1000 MPa with PSE$\geq$3·10^4 MPa $\times$ % [1]. Quenching-partitioning (Q&P) processing may provide these properties of low-alloy steels due to the formation of a multiphase structure [1]. The Q&P process consists of four steps (Fig. 1) [1–13]. Austenitization (i) followed by quenching in a hardening agent heated up to a temperature, T_q, lying below the martensite-start (M_S) and above martensite-finish (M_F) temperatures (Fig. 1) (ii) [1–4]. The quenching step prescribes the ratio between martensite and retained austenite (RA) [1–5]. The partitioning step (iii) is carried out at a temperature, T_p, for t_p. Partitioning temperature, T_p, is usually higher than M_s. This step provides the carbon partitioning from the martensite to RA. The final

cooling (iv) produces untempered/fresh martensite termed secondary martensite, M2, that may reduce the ductility of Q&P steels [9].

It was postulated [2,9,10] that the partitioning has to produce only two constituents: carbon-depleted martensite termed as primary martensite, M1, and carbon-enriched RA. Combination of high volume fraction of M1 constituent and low volume fraction of the RA can provide a high strength and considerable ductility/formability [1,3,5,7,9]. It was presumed [2,9,10] that no other accompanying processes occur and the martensite volume fraction remains essentially unchanged during this step of the Q&P process. The martensite/austenite interfaces were considered to be completely immobile after the stop of martensite growth [2,10]. However, structural characterization of low-alloy steels processed by Q&P [4–12] showed that this theoretical assumption was oversimplified. The carbon enrichment of RA that is the essential mechanism of the partitioning step overlaps with the transformation of RA into bainitic ferrite (BF) and the precipitation of transition η–Fe_2C carbides in the martensitic matrix [4–11]. In addition, an experimental evidence for the migration of the martensite/austenite interface was
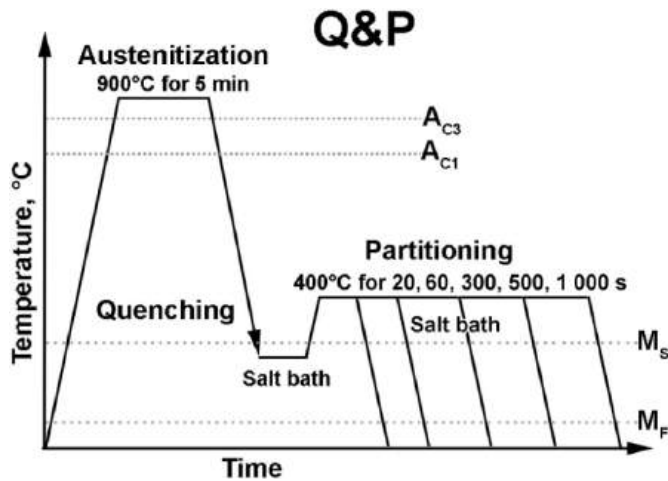
Fig. 1. Schematic graph of Q&P processing.

obtained [9]. These processes affect strongly the kinetics of carbon partitioning and mechanical properties of Q&P steels. As a result, the experimentally calculated carbon content in RA is always smaller than that predicted by theoretical models by a factor of >2 [2,9] and an unusual effect of carbon content on the mechanical properties of these steels is observed [12–14].

There exist two types of Q&P steels with different carbon content. Q&P steels belonging to the first type with ≤0.3 wt%C exhibit the PSE value of $\leq 2.7 \cdot 10^4$ MPa × % and YS ranging from 1050 to 1238 MPa [1,3, 11,13]. The second type of Q&P steels with carbon content ranging from 0.4 to 0.56 % exhibits the PSE $\geq 3 \cdot 10^4$ MPa × % and YS > 1000 MPa. Two types of Q&P steels are distinguished by morphology, volume fraction and dimension of RA, distribution of RA within the multiphase structure, and the PSE [5,7–9,11–15]. Two morphologies of RA are observed in Q&P steels [1,7–9,11–16]. Film-like RA with a thickness ranging from ~20 to ~120 nm and a length ranging from ~200 nm to ~1 μm locates at the lath and block boundaries of lath martensite structure [5,7–9,11–13]. Portion of film-like RA is significantly higher than that of blocky RA in the first type of Q&P steels. Film-like RA is highly dislocated and stable against martensitic transformation during tension [8,9,11,14,16–20]. Blocky-type RA exhibits a nearly round shape with dimensions >1 μm and locates at triple junctions or along boundaries of packets and prior austenite grains (PAG). Volume fraction of blocky RA ranges from 12 to 30 pct. and is higher than the volume fraction of film-like RA by a factor >3 in these Q&P steels [4,8,12,14, 15].

At present, the relationship between blocky RA and mechanical properties is discussed. Blocky RA transforms easily to martensite under a small strain in tension and could not contribute to ductility in transformation-induced-plasticity (TRIP) [19,20]. In addition, blocky RA can transform into a hard and brittle M2 martensite constituent during final cooling that also deteriorates ductility [9]. However, high values of the PSE are attributed to the transformation of blocky RA enriched by carbon to strain-induced martensite under tension in Q&P steels [8,14–17,21]. There is a contradiction concerning the role of blocky RA in ductility that could be attributed to phase transformations during partitioning and their effect on structure and mechanical properties. It is known [19,20,22] that bainitic transformation leads to subdivision of austenite by sheaves of bainitic ferrite to lamellas, and this structure is optimal for achieving a good combination of strength and ductility. It seems that carbon content in RA with different morphology plays a crucial role in the mechanical behavior of Q&P steels. The effects of blocky RA on the PSE of TRIP steels, in which the carbon contents of RA and the bulk are nearly the same [16,19,20], and Q&P steels with carbon-enriched RA [4,8,9,12,14] are distinctly different.

The effect of partitioning on multiphase microstructure and mechanical properties was reported for the first type of Q&P steels [6,7,13]. In contrast, the same studies dealing with the second type of Q&P steels are limited [8,12] despite the fact that there is a strong correlation between phase transformation during partitioning and mechanical properties [4,8,12,23,24]. The main purpose of the present work is to consider the microstructural evolution and its relation with the mechanical properties of low-alloyed steel with 0.44 wt%C during partitioning. The second objective of this work is to reveal features of bainitic transformation occurring in blocky RA in order to understand the role of this phase in achieving superior values of the PSE in the second type of Q&P steels [8,14].

2. Experimental procedure

A Fe-0.44%C-1.81%Si-1.33%Mn-0.82%Cr-0.28%Mo (in wt.%) steel was produced by air induction melting followed by electro-slag remelting. The steel was subjected to solution treatment at 1150 °C for 4 h followed by forging at temperatures decreasing from 1150 to 950 °C [8]. Samples with a 3 mm thickness were cut from the forged billet and austenitized at 900 °C for 5 min, followed by quenching in a salt bath at $T_q = 200$ °C for 15 s (Fig. 1). Next, samples were carried from this bath to the other one heated up to $T_p = 400$ °C. Partitioning was performed with the holding times $t_p = 20, 60, 300, 500$ and 1000 s followed by air cooling (Fig. 1). The critical points of the present steel ($M_S = 270$ °C and $M_F = 51$ °C) were reported in previous work [8] and, therefore, $M_F < T_q < M_S$, and $T_p > M_S$. The quenching temperature was chosen based on data from previous work [8], which showed that the highest PSE was attained in this steel at $T_q = 200$ °C.

The flat specimens with a gauge length of 35 mm and cross-section of 7×3 mm² were cut from samples processed by the Q&P route with different partitioning times (Fig. 1) and then tensioned using the «Instron 5882» testing machine at room temperature in accordance with ASTM E08M − 04 standard. Hardness was measured using a Wolpert Wilson 600 MRD tester in accordance with the ASTM E18 standard.

The microstructure was examined using a Quanta 600 FEG scanning electron microscope (SEM) equipped with an electron backscatter diffraction (EBSD) pattern analyzer incorporating an orientation imaging microscopy (OIM) system and a JEOL JEM-2100 transmission electron microscope (TEM) equipped with an INCA energy dispersive X-ray spectrometer (EDS). SEM and TEM observations were carried out using samples polished with 10 % $HClO_4$ and 90 % CH_3COOH solution. Average dimensions of particles were calculated from measurements of at least 50 particles on selected TEM images. The particle density of carbides was measured by counting the number of the particles from the bright-field TEM images. Identification of carbides was carried out using both analyses of selected area electron diffraction patterns at thin foils and chemical composition by EDS technique using the extraction carbon replicas obtained by techniques described in work [25]. The volume fractions of the carbide particles were estimated by measuring their projected area fraction on SEM images. The statistical error did not exceed 15 %.

The OIM images were subjected to a clean-up procedure, setting the minimal confidence index to 0.1. These misorientation maps were analyzed by TSL OIM Analysis 6 and MTEX 5.8 parent grain reconstruction algorithm assuming Kurdjumov–Sachs (K–S) orientation relationship between parent austenite and formed martensite [14,26] that allows calculating dimensions of PAGs, packets by linear intersection method. Block widths were measured using the reconstructed EBSD maps by calculating the projection of all boundary points to the normal of the habit plane trace of the $\{111\}_\gamma \| (011)_\alpha$ in the PAGs [14,26]. Only blocky-type RA was detected by the EBSD technique due to the fact that the dimensions of film-like RA are smaller than the accuracy of this technique. TEM micrographs were used for measurement of the transverse lath sizes and thickness of film-like RA by the linear intercept method.

Densities of lattice dislocations were calculated from EBSD data using Kernel average misorientation (KAM) as [11]:

$$\rho_{KAM} = \frac{2\theta_{KAM}}{b \bullet h} \tag{1}$$

where b is the Burgers vector, the distance h corresponds to the step size of the scanning. The ρ_{KAM} value characterizes the elastic bending of the crystal lattice and, therefore, the internal elastic stress field originated from lattice dislocations [27]. The density of the lattice dislocation was estimated by counting the individual dislocations crossing the thin foil surfaces on TEM micrographs:

$$\rho_{TEM} = \frac{N}{A} \tag{2}$$

where N is the number of dislocations, and A is the selected area. At least ten arbitrary selected bright-field images taken under multiple-beam conditions were studied to ensure statistical reliability of the data.

The volume fraction of RA was determined by means of magnetic saturation measurements using a Fischer Feritscope FMP30 and X-ray analysis using a Rigaku Ultima IV diffractometer (40 kV, 40 mA). Spectra were taken in the range of 2θ Bragg angle from 30 to 135°, with a step size of 0.02 deg. A X'pert High Score Plus software was used to calculate the volume fraction of RA according to the peaks intensities for the fcc lattice: $(200)_\gamma$, $(220)_\gamma$, $(311)_\gamma$ and the bcc lattice: $(200)_{\alpha'}$, $(211)_{\alpha'}$,

$(220)_{\alpha'}$ [8,11,23,25,28–30]. The average concentration of carbon in RA was calculated using the following relationship [8,27,28]:

$$\alpha_\gamma\left(\overset{\bullet}{A}\right) = 3.578 + 0.033 C_{RA} + 0.00095 Mn_{RA} + 0.0031 Mo_{RA} \tag{3}$$

where C_{RA}, Mn_{RA}, and Mo_{RA} are the concentrations of C, Mn, and Mo in RA in wt.%, respectively.

A high-precision Bahr DIL 805 A/D dilatometer was used to obtain dilatations curves using cylindrical samples with a 10 mm length and a 3 mm diameter. The dilatation samples were heated from room temperature to 900 °C with a heating rate of +10 °C/s and held at this temperature for 10 min. Next, the samples were cooled in helium from 900 to 250 °C with a cooling rate of −50 °C/s followed by cooling to 200 °C with a cooling rate of −14 °C/s. The samples were held at 200 °C for 15 s and then heated up to 400 °C with a heating rate of +50 °C/s. Samples were held at 400 °C for 60, 500, and 1000 s. Final cooling to ambient temperature was carried out with a cooling rate of −5 °C/s. Other details of experimental procedures were reported in previous works [8,11,14]. Volume fractions of the M1 and M2 constituents, bainite were calculated by applying the lever rule and using the linear expansion coefficient of the fcc and bcc lattices reported in works [11, 14,31] taking into account the volume fraction of RA calculated from X-ray diffraction data.

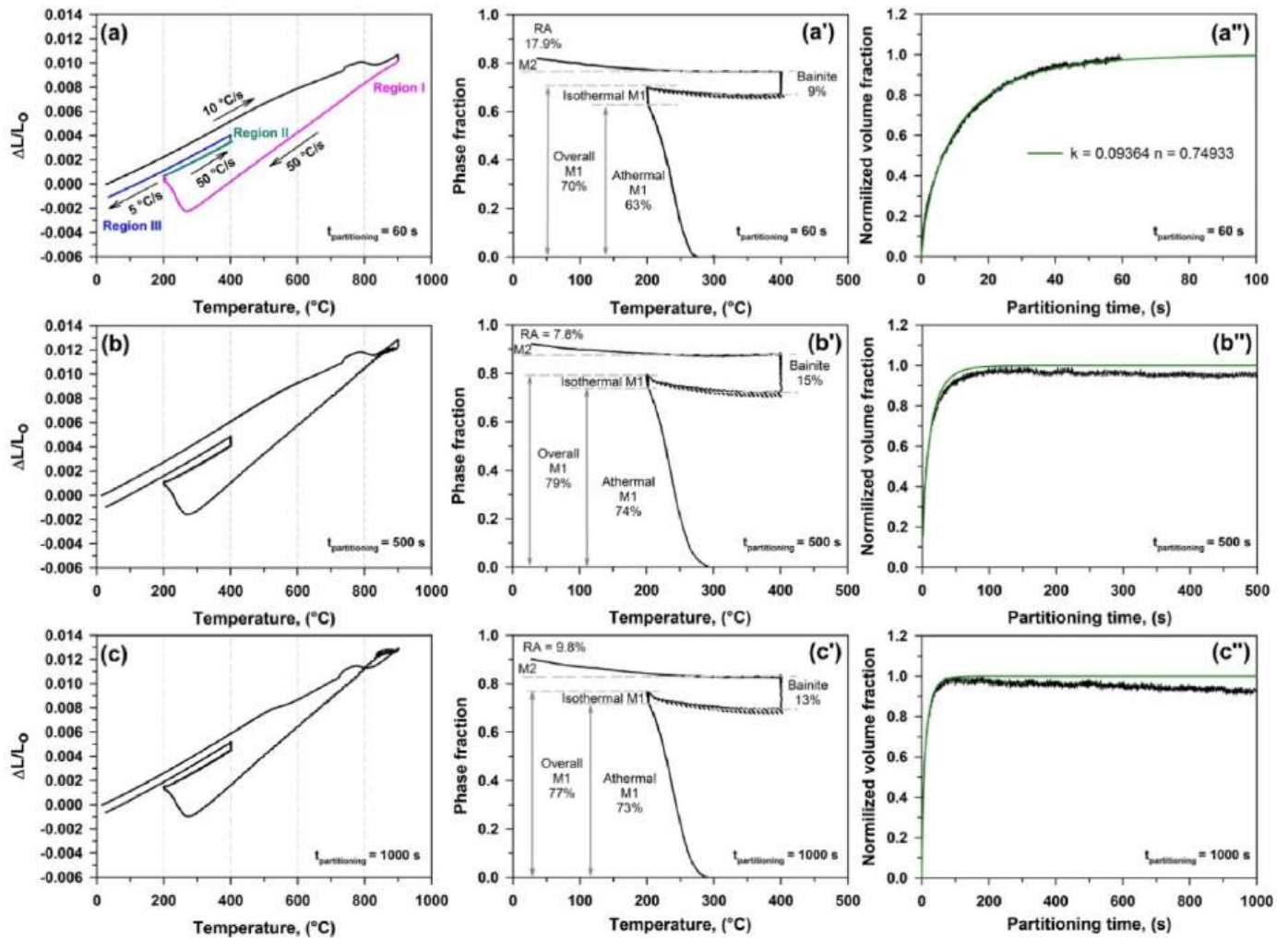The Thermo-Calc software (Ver. 5) with the TCFE7 database was

Fig. 2. Dilatation curves of the steel austenitized at 900 °C and quenched to 200 °C followed by partitioning at 400 °C for 60 s (a), 500 s (b), and 1000 s (c) with final air cooling to room temperature; relative change in length versus temperature obtained during Q&P processing for these samples (a', b', c'), relative length change *vs* time (a", b", c").

used for calculation of Gibbs energies and thermodynamically equilibrium compositions of different phases.

3. Results and discussion

3.1. Phase analysis

3.1.1. Dilatometry

A dilatation curves are shown in Fig. 2. Phase transformations occurring during Q&P processing and affecting contraction or expansion are represented schematically in Fig. 3. The volume fractions of the M1 and M2 constituents and bainite are presented in Table 1. Three dilatation regions associated with three aforementioned steps of Q&P processing (Fig. 1) are distinguished (Fig. 2) [7,31]. Region I involves the austenitization at 900 °C followed by quenching. This region is similar for all dilatation curves. A strong volume expansion due to the formation of athermal martensite takes place during cooling in the temperature range M_S-T_q (Fig. 3). Significant scattering in the volume fraction of athermal martensite calculated from dilatation data is observed (Fig. 2a'-c', 3, Table 1). A modified Koistinen-Marburger (K-M) equation was suggested to calculate the volume fraction of untransformed austenite at a certain T_q [32]:

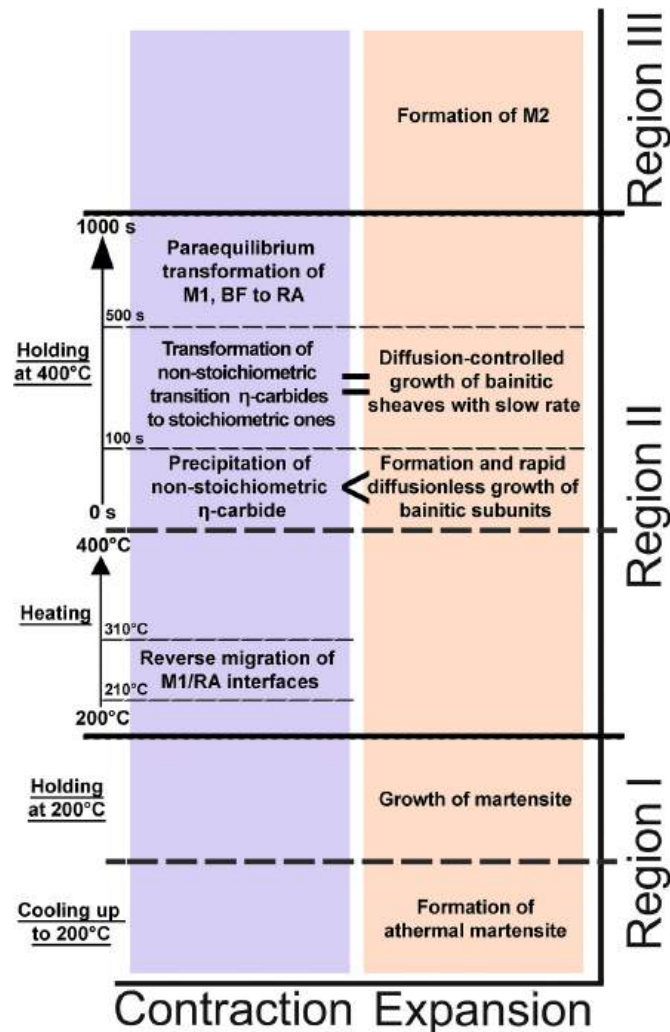$$f_{\alpha'} = 1 - \exp\left(-\alpha(M_s - T_q)\right) \tag{4}$$

Fig. 3. Phase transformations and their effect on dilatation during Q&P processing.

$$\alpha = \left(27.2 - (0.14Mn + 0.21Si + 0.11Cr + 0.05Mo) - 19.8(1 - \exp(-1.56C))\right) / 10^3 \tag{5}$$

where the concentrations of carbon, manganese, chromium, molybdenum, and silicon are in wt.%. The modified K-M equation provides a M1 volume of 69 %, and we will use this theoretical value as an averaged experimental one as the volume fraction of athermal martensite (Table 1).

Volume expansion occurs during isothermal holding at T_q that is indicative for the formation of an additional volume fraction of the bcc phase (Fig. 2). It is known [14,24,33–38] that volume expansion can be attributed to the superposition of several different processes, including carbon enrichment of RA, bainitic transformation, and isothermal martensitic transformation. The feasibility of carbon partitioning could be evaluated by calculating diffusion distances in bcc and fcc phases using the following equation [34]:

$$t = \frac{\overline{X}^2}{6D} \tag{6}$$

where $\overline{X}$ is the average diffusion distance, $D = D_0 \exp(-Q/RT)$ is the diffusion coefficient of carbon in α/γ−Fe ($D_0^\alpha = 0.62 \cdot 10^{-6}$ m^2/s, $D_0^\gamma = 0.109 \cdot 10^{-4}$ m^2/s [39]), Q is the activation energy for carbon diffusion in α/γ−Fe ($Q_\alpha = 80.4$ kJ/mol, $Q_\gamma = 135.7$ kJ/mol [39]), R is the gas constant, and T is the absolute temperature. The $\overline{X}$ values for ferrite and RA was evaluated as 284 nm and 1 $\mathring{A}$, respectively, at $T_q = 200$ °C and duration of quenching step (15 s). Therefore, isothermal holding at 200 °C for 15 s is not sufficient for the carbon partitioning from martensite to RA (Fig. 3) and the carbon enrichment of RA has no sense to the volume expansion. At T = 300 °C and a holding time of 1 s the $\overline{X}$ value for austenite was calculated as 2 nm and, therefore, carbon enrichment of a thin layer near the α'/γ interface may occur during heating from T_q to T_p. The effect of partitioning time on $\overline{X}_\alpha$ and $\overline{X}_\gamma$ values is summarized in Table 2. The diffusion rate of carbon in austenite was calculated at 280 and 400 °C to evaluate the rate of carbon enrichment of the thin layer in untransformed austenite adjacent to the α'/γ interface.

Volume expansion during isothermal holding at T_q could be attributed to the isothermal transformations [34–38]. The nature of the isothermal transformation at $T_q < M_S$ is still poorly known, and several mechanisms were suggested to explain the formation of the isothermally transformed phase with bcc lattice [36–38,40]. It is worth noting that isothermal martensite transformation was found in hypereutectic steels or medium-carbon steels with a high Ni content, initially [38,41]. The occurrence of this type of displacive transformation was reported in a limited number of works for low-alloyed hypoeutectoid steels, and the conditions at which it takes place are now under debate [34–37,41,42]. M.J. Santofimia et al. [36] suggested that the volume expansion could be attributed to the continued growth of the pre-existing athermal martensite or the isothermal nucleation and growth of martensite during partitioning. The growth of pre-existing martensite by migration of the α'/γ interface occurs if the austenite carbon content is depleted relative to the equilibrium value [42,43] that takes place at T_q. S. Samanta et al. [35] noticed that the occurrence of isothermal martensite transformation through nucleation of the martensite embryos followed by their fast growth is not possible in a low-alloyed steel with 0.32 wt%C at a temperature of 210 °C that is below M_S. It is worth noting that bainitic transformation occurring at $T < M_S$ may also provide the volume expansion [35]. However, S. Kim et al. [40] proposed that no transformation of RA to bainite may occur if the partitioning temperatures ≤250 °C. It is well known [22] that the formation of bainite leads to carbon enrichment of RA that could not occur, as it is resulted from the analysis of Eq. (6). Therefore, the occurrence of bainitic transformation at 200 °C is impossible. The continued growth of athermal martensite is a single mechanism of isothermal transformation that may occur at this

Table 1

Phase volume fractions of the Fe-0.44C steel after different partitioning times. Volume fractions of athermal martensite, isothermal martensite, overall M1 constituent and $M1_{bp}$ structural component were averaged as 69, 5, 74 and 70 %, respectively.

Partitioning time, s	Phase Volume Fractions, %								
	Athermal M1	Isothermal M1	Overall M1	$M1_{bp}$ before partitioning	RA before partitioning	RA (X-Ray)	RA (magnetic saturation)	M2	Bainite
60	63	7	70	68	32	17.9	17.9	5	9
500	74	5	79	72	28	7.5	7.5	5	15
1000	73	4	77	70	30	9.8	10.2	7	13

Table 2

Effect of partitioning time on average size of RA, calculated by EBSD technique, thickness of RA, and primary martensite/bainite, determined from Fig. 5, and the average diffusion distances in BCC, $\overline{X}_\alpha$, and FCC, $\overline{X}_\gamma$, lattices (Eq. (6)), carbon concentration in RA (X-ray) and M1 constituent (Eq. (12)).

Partitioning time, s	Size of RA, μm	Thickness of RA/M2 areas, nm	Thickness of M1/bainite areas	$\overline{X}_\alpha$, μm	$\overline{X}_\gamma$, nm	wt. %C in	
						RA	M1
20	1.89	249 ± 17	1.00 ± 0.13	6.5	186	1.37	–
60	2.65	446 ± 27	0.99 ± 0.15	11.2	325	1.38	0.2
300	3.16	415 ± 57	1.00 ± 0.11	25.2	726	1.38	–
500	1.03	238 ± 16	1.07 ± 0.12	32.5	938	1.43	0.39
1000	1.63	419 ± 31	1.15 ± 0.13	46,0	1323	1.63	0.3

low temperature (Fig. 3) [36,42,43].

It was shown in previous work [44] that isothermal holding at 200 °C for 15 s is extremely short for precipitation of transition carbides, and, therefore, no difference between the carbon content in athermal martensite and isothermal martensite could be expected. It is known [22] that transition carbides grow by a displacive mechanism, and, therefore, the strain energy associated with the growth of martensite crystals has to affect a dispersion of these carbides precipitated during partitioning in athermal martensite and isothermal martensite if these structural components are distinguished by long-range distortions over the whole laths. However, the difference in the two microstructures is inessential [41], and, therefore, at any partitioning conditions, the precipitation processes occurring in these two structural components are expected to be essentially the same. As it will be shown below no remarkable difference in the dispersion of transition carbides between martensite structural elements was found after partitioning. Thus we presume that the effect of these two different components on mechanical properties will be essentially the same, and the martensitic phases evolved during cooling from M_S to T_q, and isothermal holding at T_q implies the M1 constituent. Therefore, the total volume fraction of primary martensite after quenching pass is a sum of the volume fraction of athermal martensite and continuously grown martensite evolved during isothermal holding (Fig. 3, Table 1).

Region II involves heating from 200 to 400 °C and partitioning at 400 °C with durations of 60, 500, and 1000 s (Figs. 2 and 3) [7,31]. A distinctive feature of the present steel is a significant net volume contraction during heating from ~210 to ~310 °C (Fig. 2a'-c'). It is known that the volume contraction could be attributed to precipitation of transition carbides, carbon depletion from martensite and reverse transformation of RA into martensite [14,18,24,31,33,36,45]. It was shown in previous works [25,44,46] that at T ≤ 280 °C, the precipitation of transition carbides occurs slowly, and, therefore, heating from 210 up to 310 °C during for 2 s is insufficient for this phase transformation. Inspection of Eq. (6) showed that no depletion of carbon from martensite could occur since the thickness of the carbon enriched layer in untransformed austenite near the α'/γ interface is ~2 nm. However, it is known [9,42,43,47,48] that the formation of this thin layer provides reverse migration of the α'/γ interface from the untransformed austenite to the martensite. This reverse migration could contribute to the volume contraction (Fig. 3). Martensite/austenite interfaces are feasible for bi-directional migration martensite ↔ untransformed austenite. Direct migration takes place if the carbon concentration in this layer is smaller relative to equilibrium, and reverse migration occurs if the actual carbon

concentration approaches equilibrium in the layer [9,10,42,43,48]. Interface migration occurs at a higher rate (~10^{-4} ms^{-1} [41]) than carbon enrichment of the layer in untransformed austenite (~$2 \cdot 10^{-9}$ ms^{-1}) that causes bi-directional migration of the α'/γ interfaces [9,48]. Migration of the α'/γ interfaces to untransformed austenite or martensite contributes to the volume expansion and contraction, respectively [9,10,42,43]. The volume expansion and contraction occur consequently, that leads to oscillations on dilation curves (Fig. 2a'-c'). These oscillations are observed during heating up to T_p but the volume contraction net ends at 310 °C (Fig. 2a'-c').

Thus the direct migration of the coherent martensite/austenite interfaces provides isothermal transformation of austenite to martensite during isothermal holding at T_q and the reverse migration leads to a small decrease in the volume fraction of the M1 constituent during heating from 210 to 310 °C (Fig. 2a'-c', Table 1) revealed as the net volume contraction. This fact is in contrast with the data reported in work [35]. The highest temperature, at which the oscillation was detected, is ΔT~130K higher than M_S. It is worth noting [49] that isothermal martensite may evolve at temperatures higher than the M_S.

During the partitioning step, significant volume expansion was observed (Fig. 2). The dependence of dilatation on partitioning time (Fig. 2a''-c'') is highly specific. Volume expansion takes place at small partitioning times ≤100 s (Fig. 2a''-c''). The increment in sample length tends to decrease with time approaching a plateau at t_p ~100 s. This dependence of volume expansion on partitioning time is typical for low-alloy steels with C ≤ 0.34 wt% [4,7,11,14,31,34–38,40]. At t_p > 100 s, the net volume contraction is observed up to 1000 s (Fig. 2a''-c''). Oscillations on the dilatation curves indicate the sequential occurrence of volume expansion and contraction during partitioning (Fig. 2a'-c'). The same type of dilatation curves was reported for a 0.49 wt%C steel [24] and low-carbon Q&P steels partitioned at T ≥ 400 °C [31,40].

At T_p > M_S, the carbon enrichment of RA and bainitic transformation could contribute to the overall volume expansion only [4,7–12,14,24, 33–36,40,42,45]. The contribution of the first process to the net expansion is negligible, and, therefore, the volume expansion during isothermal holding can be directly related to bainitic transformation (Fig. 3) [11,12,18,37,40,45]. It is worth noting that our calculations using the equations reported in works [34,50] (not presented here) confirmed that the contribution of carbon enrichment to the overall volume expansion is less than 1 %. No sudden increase in the rate of volume expansion [40] was found (Fig. 2a'- c') and, therefore, the onset of bainitic transformation takes place without an incubation period. It is known [9,31,35,38,51] that pre-existing martensite strongly accelerates

bainitic transformation, providing its high rate during partitioning. The α'/γ interfaces act as preferential nucleation sites for the formation of bainitic subunits, and no incubation period for bainitic transformation is observed in Q&P steels if the volume fraction of martensite is high enough [7,9,37,38,51–54]. We could postulate that only bainitic transformation contributes to the volume expansion up to 100 s partitioning. The volume fraction of BF calculated from dilatation curves is presented in Table 1.

Bainitic transformation occurs due to carbon partitioning from BF to the RA [22,41]. Therefore, at T_p, carbon partitioning from both martensite and BF to untransformed austenite occurs concurrently. Carbon enrichment of RA stabilizes untransformed austenite and the bainitic transformation stops [7,9,22,40,41,51,54]. The carbon concentration in austenite, at which the bainitic transformation eventually comes to a halt, could be evaluated from the equality condition of the bainite-start temperature, B_S, and T_p. It was suggested [32] that the bainite-start temperature, B_S, can be calculated by the empirical formula:

$$B_S (°C) = 839 − 86\%Mn − 67\% Cr − 75\%Mo - 23\% Si - 270 \cdot (1 − \exp(−1.33\% C)) \tag{7}$$

where the concentrations of substitutional and interstitial elements are in wt.%. Eq. (7) provides superior correlation between calculated and experimental bainite-start temperatures for steels with C < 1 wt% and Si additions [32]. No partitioning of substitutional solutes was taken into account for calculation of the bainite-start temperature since these elements are unable to redistribution at 400 °C for ≤7200 s [51] and bainitic transformation occurs in paraequilibrium condition [22,41]. $B_s = 570$ °C was calculated for carbon bulk composition (0.44 wt%) and bainitic transformation could occur with a high rate at T_p if carbon content in austenite and carbon bulk composition are nearly the same. $B_S^1 = 408$ °C was calculated for 1 wt %C and, therefore, carbon enrichment of RA up to this value suppresses the bainitic transformation [7,14,52]. RA with a carbon content >1 wt %C is thermodynamically stable during partitioning at 400 °C. Shan Chen et al. [51] also reported that 1 wt%C ceases the transformation of RA to bainite. It is known [7,10,22] that partitioning produces a wide distribution of carbon concentrations over crystals of RA, and bainitic transformation could occur in blocks or films of RA with a carbon content ≤1 wt%, only. Therefore, at t_p ~100 s, the stop of bainitic transformation occurring with a high rate at low partitioning times (Fig. 2a''-c'') is attributed to the enrichment of the RA areas adjacent to the martensite/austenite interfaces up to >1 wt%C.

Tempering of the M1 constituent occurs during partitioning that leads to the volume contraction [5–9,11,12,24,31,34,54,55]. At t_p > 100 s, the net dilatation during partitioning is a superposition of bainitic transformation providing the volume expansion [9,31,37,51,53,54] and precipitation of transition carbides providing the volume contraction [24,34,49,54] (Fig. 2a''-c'', 3). At t_p > 60 s, the volume fraction of bainite calculated from dilatometry is apparent due to the fact that bainitic transformation overlaps with precipitation of transition carbides. So dependencies of the M1 constituent on partitioning time are imaginary since the quenching regime is the same. In the partitioning time interval 100–500 s the bainitic transformation slows down (Fig. 2b'',c'') that could be attributed to the transition from fast growth of subunits through a diffusionless mechanism to diffusion-controlled growth of sub-unit aggregates called sheaves [9,22,41]. Growth of sheaves occurs slowly [22,41]. The volume fraction of bainite calculated under the assumption that the whole increment in specimen length is attributed to the formation of bainite provides a superior balance of structural constituents (Table 1) [56]:

$$f_{M1} + f_B + f_{M2} + f_{RA} = 1 \tag{8}$$

where f_{M1}, f_B, f_{M2}, f_{RA} are the volume fractions of primary martensite, bainite, secondary martensite, and RA, respectively. This balance of structural components could be attained if the volume contraction

attributed to the precipitation of transition carbides accompanied by carbon depletion of the martensitic matrix [34] is compensated by the volume expansion attributed to carbon enrichment of RA [50].

Bainitic transformation providing the volume expansion ends at t_p ~500 s (Fig. 2b–b'', c-c'', 3). Further partitioning leads to an increase in the volume fraction of RA. At 400 °C, the Gibbs energies for two phases (fcc and bcc) were calculated for austenite with a carbon content of 1.6 wt% (Table 2) and ferrite with a carbon content of 0.0004wt.%, that is thermodynamically equilibrium value at T_p are −23 948.0 J/mol and −28 123.9 J/mol, respectively. As a result, the growth of the austenite phase controlled by carbon diffusion could occur in a paraequilibrium manner without redistribution of substitutional solutes through a displacive mechanism due to migration of semi-coherent or coherent bcc/fcc interfaces (Fig. 3) [2,7,9,22,41–43]. A decrease in the volume fraction of bainite (Table 1) and oscillations on dilatation curves attributed to bi-directional migration of the interfaces support this conclusion.

In Region III, the formation of secondary martensite is observed (Fig. 2a'-c', 3). The martensite start temperature for the M2 was calculated as ~200 °C from the dilatation curves. Therefore, the M_S for the M2 constituent is ΔT = 70 K lower than the M_S for the bulk. The volume fractions of the M2 constituent after 60 and 500 s partitioning are essentially the same (Table 2). Increasing the duration of partitioning from 500 to 1000 s leads to an increase in the volume fraction of secondary martensite (Fig. 2b',c'). The carbon concentration in the M2 constituent could be evaluated from the M_S for secondary martensite. Several empirical relationships were developed to estimate the effect of steel chemical composition on the M_S [32,57–60]. Three equations suggested by S.M.C van Bohemen [32], K. W. Andrews [59], and C. Capdevila et al. [60] were used for the prediction of M_S^B, M_S^A, M_S^C temperatures, respectively:

$$M_S^B ((\hat{o}) C) = 565 − 31Mn − 10Cr − 12Mo − 13Si − 600 \, exp(1 − exp(−0.96C)) \tag{9}$$

$$M_S^A (°C) = 539 − 423C − 30.4Mn − 12.1Cr − 7.5Mo − 7.5Si \tag{10}$$

$$M_S^C (K) = 764.2 − 302.6C − 30.6Mn − 8.9Cr − 14.5Si + 2.4Mo \tag{11}$$

where the concentrations of carbon, manganese, chromium, molybdenum, and silicon are in wt.%. M_S^B (°C) = 287 °C, M_S^A (°C) = 282 °C and M_S^C (K) = 561 K (288 °C) were calculated for the bulk carbon content. Equations (10) and (11) provide superior mutual correlation but overestimate the M_s experimental value at ΔT~18 K. Equation (9) overestimates the experimental martensite start temperature at ΔT~12 K. These equations predict the martensite-start temperature for secondary martensite M_S^{M2} ~25 °C if the enrichment of RA attains 1.4 wt%C. Therefore, no formation of the M2 constituent can occur if RA is enriched by carbon up to 1.4 wt%C.

We will use three empirical formulas (Eqs. 9–11) to calculate the carbon enrichment of the M2 constituent, taking into account $M_S^{M2} = 200$ °C obtained from dilatation curves. We use $M_S^{M2} = 218$ °C for calculation of the carbon concentration in the M2 constituent taking into account the overestimation by Eqs. (10) and (11). Carbon concentration in the M2 constituent was calculated by Eq. (9) using $M_S^{M2} = 212$ °C. Eqs. (9)–(11) predict the carbon contents of 0.64, 0.60, and 0.67 wt%, respectively. These data confirm the heterogeneous carbon distribution in RA after partitioning [7,10]. Partitioning produces a wide distribution of carbon concentrations over the crystallites of blocky RA [10], and areas of RA with carbon content ranging from ~0.64 to ~1.4 wt% could transform into the M2 constituent under final cooling. We averaged these values to 0.9 wt%C for calculation of carbon concentration in primary martensite, C_{M1} (Table 2), by the mass balance of carbon [14,53]:

$$C = f_{RA}C_{RA} + f_{M2}C_{M2} + f_B C_B + f_{M1}C_{M1} \qquad (12)$$

where C_{M1}, C_{M2}, C_B, and C_{RA} are the carbon concentration in primary martensite, including transition carbides located in the matrix of this constituent, secondary martensite, BF, and RA (Table 2), respectively, C = 0.44 wt% is the carbon content in bulk steel. The C_B value was taken as 0.03 wt%C [53]. A volume fraction of RA calculated by X-ray techniques was taken. Inspection of Table 2 shows that carbon concentration in the M1 constituent increases with increasing partitioning time from 60 to 500 s and then decreases. Values of $\overline{X}_\gamma$ (Table 2) are indicative that full carbon partitioning from martensite/BF to untransformed austenite could occur during partitioning at $t_p \geq 60$ s. Therefore, almost the whole carbon concentration in the M1 constituent (Table 2) is consumed for the formation of transition carbides upon 500 s partitioning (Fig. 3). Further partitioning leads to partial dissolution of the transition carbides.

3.1.2. X-ray analysis and magnetic saturation measurements

The effect of partitioning time on the volume fraction of RA and the carbon concentration in this phase are presented in Fig. 4 and Tables 1 and 2 The X-ray technique and magnetic saturation measurements showed a good mutual correlation in the determination of the RA volume fractions after 60, 500, and 1000 s (Fig. 4a and Table 1), while after 20 and 300 s the volume fractions of RA determined by X-ray analysis are significantly smaller than those obtained from magnetic saturation data. The reason for this difference in the volume fractions of RA determined by these techniques was considered in recent work [25] in detail. It is seen that the effect of partitioning time on the volume fraction of RA in the 0.44 wt%C steel is unique. The volume fraction of RA tends to decrease or remains virtually unchanged with increasing partitioning time in Q&P steels with ≤0.3 wt%C [6,7,13]. In contrast, in the present steel the volume fraction of RA continuously increases up to 60 s partitioning and then decreases in the time interval 60–500 s (Fig. 4a). Next, the volume fraction of RA increases in the time interval 500-1000 s (Fig. 4a). It is worth noting that nearly the same effect of partitioning time on RA volume fraction was reported in work [36], but changes in the RA volume fraction presented in this work were within the range of measurement errors.

The carbon concentration of RA remains essentially unchanged up to $t_p \sim 300$ s and increases from 1.38 to 1.63 with increasing partitioning time from 300 to 1000 s (Table 2). The volume fraction of RA before partitioning could be evaluated from the balance of structural components (Eq. (8)) as $f_{RA} = 100 - f_{M1\,bp}^{overall} \sim 32$ % (Table 1). Upon $t_p \sim 20$ s a minor portion of RA transformed to bainite (6 % from Fig. 2a"). Upon $t_p \sim 60$ s the portion of RA transformed into bainite during partitioning becomes higher than that transformed into the M2 constituent during final cooling (Table 1). A major portion (~56 %) of untransformed austenite presented in structure before partitioning retains after final cooling due to carbon enrichment (Table 2). No substantial discrepancy

between the volume fraction of the M2 constituent and bainite determined by dilatometry and from the balance of structural components (Eq. (8)) was found (Table 1).

Increasing partitioning time up to 100 s decreases this portion to 48 % due to the transformation of austenite to bainite (Fig. 2b",3). It is seen (Table 1) that the volume fraction of secondary martensite is nearly independent on partitioning time, and, therefore, bainitic transformation is the main mechanism providing a strong decrease in the volume fraction of RA with increasing partitioning time from 60 to 500 s. The carbon concentration in RA tends to increase with increasing volume fraction of martensite/bainite (Tables 1 and 2) [2,61]. Therefore, bainitic transformation promotes carbon enrichment of RA in structure with a high volume fraction of pre-existing martensite in the same manner as in steels with fully austenite initial structure [22,41] due to the increasing volume fraction of BF with increasing t_p. At $t_p >$ 500, the growth of austenite occurs at the expense of martensite with an average carbon content of ~0.32 wt%C (Table 2). An increase in carbon content of RA (Table 2) could take place due to carbon flux from the transition carbides located in the M1 constituent to austenite only. The growth of untransformed austenite and progressive carbon enrichment of this phase lead to partial dissolution of η-Fe$_2$C carbides and/or carbon depletion from these carbides to austenite through martensitic matrix.

3.2. Effect of partitioning on microstructure

Primary martensite and BF are distinctly distinguished from areas of secondary martensite/RA at SEM micrographs as heavily and slightly etched constituents associated with carbon-depleted and carbon-enriched phases, respectively (Fig. 5) [14,22,28,51,62]. The M2 component is poorly distinguished from RA by SEM observations (Fig. 5). The M2/RA islands may exhibit irregular or rectangular shapes in dependence on partitioning time and usually locate at packet boundaries or block boundaries if a coarse packet contains one block [44]. The M1 constituent is distinguished from BF by the presence of carbides. Carbides exhibiting a plate-like shape are observed in the M1 constituent. The difference in a dispersion of carbides between these two phases is useful for identification of bainite at SEM microstructure. As it was shown above, the displacive mechanism of carbide formation is dependent on the elastic energy of a bcc phase [22]. A strong difference in lattice distortions between martensite and BF was detected by Kernel misorientation maps (not shown here) in the present study. As a result, the driving force for precipitation of transition carbide in martensite during tempering is significantly higher than that in BF [22]. Carbide-free BF evolves in Si-rich low-alloyed steels [1,3,9,22,55]. Islands of secondary martensite and RA containing no carbides [28,51, 62] could be recognized by SEM observations as units (Fig. 5).

The difference in etched relief between the M1 constituent and the M2/RA islands on SEM micrographs is dependent on partitioning time (Fig. 5). After 20 s partitioning the M2/RA islands are poorly recognized (Fig. 5a) and, therefore, no significant carbon partitioning took place
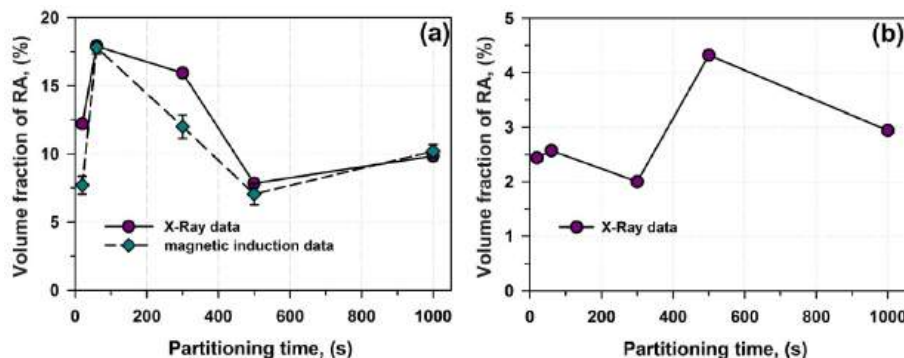

Fig. 4. Effect of partitioning time on volume fraction of RA (a), portion of RA after tension (b).
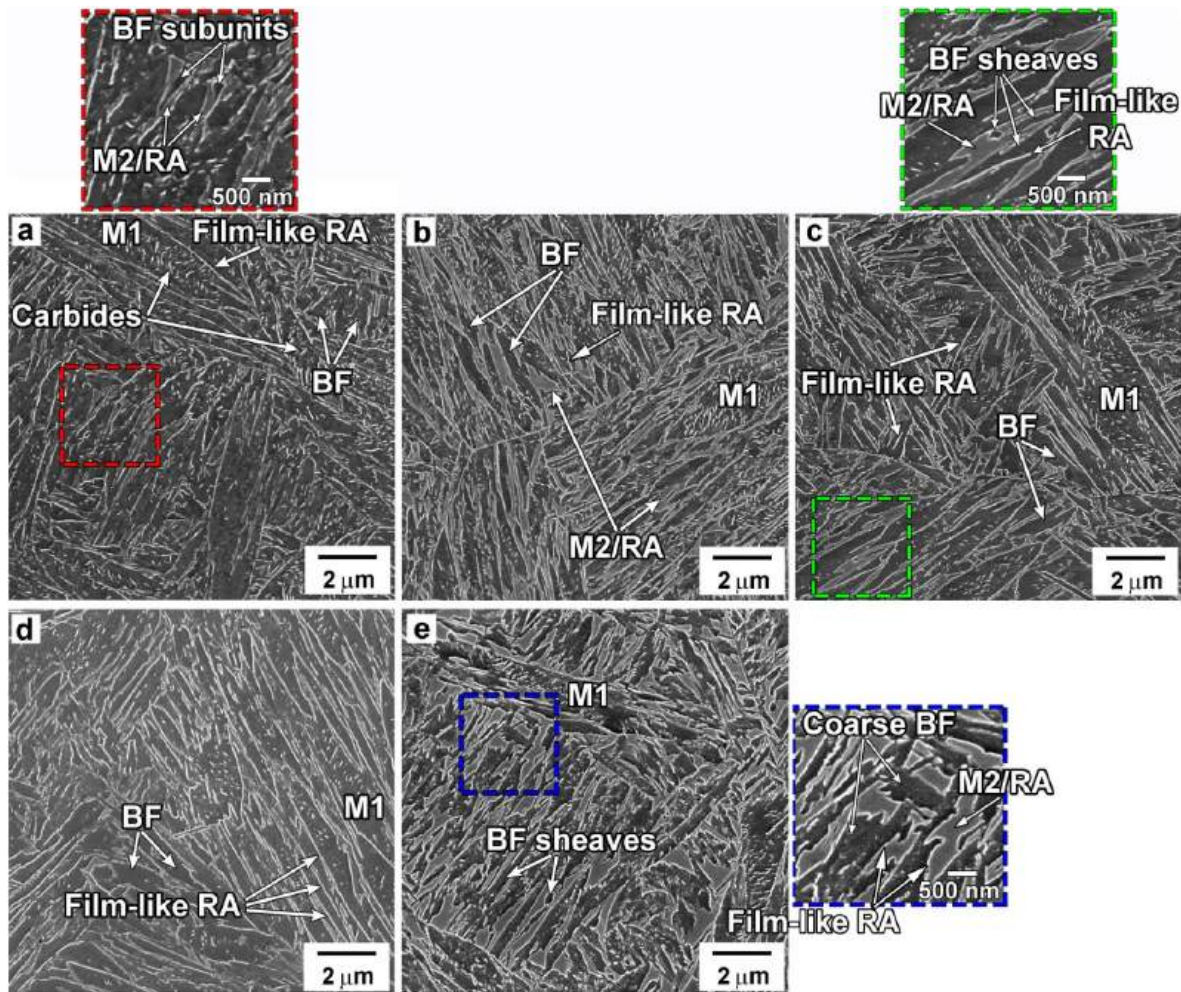
Fig. 5. SEM micrographs of the Fe-0.44C steel after partitioning time of 20 s (a), 60 s (b), 300 s (c), 500 s (d), and 1000 s (e).

between the M1 constituent and these islands. Only separate thin M2/RA islands are well-distinguished. These islands exhibit a plate-like or irregular shape with a small thickness. The volume fraction of these islands is low. In addition, the film-like RA could be distinguished at the packet boundaries. The average diffusion distances, $\overline{X}_\alpha$ and $\overline{X}_\gamma$ calculated for martensite and RA using Eq. (6), are significantly higher and lower than dimensions of martensite and RA, respectively (Table 2). The $\overline{X}_\gamma$ value is enough to provide homogeneous carbon distribution in the film-like RA (Fig. 6a and b, Table 2) [8,11,14,62] and no transformation of this type of RA to secondary martensite is expected. The film-like RA located at block boundaries exhibits more bright contrast than blocky RA due to carbon enrichment and homogeneous distribution of this interstitial solute within this type of RA (Fig. 5a). Only ~200 nm layers adjacent to the martensite/austenite interfaces could be enriched by C ≥ 1.4 wt% (Table 2). As a result, the periphery of the RA blocks retains untransformed after cooling [45] and the core regions of the RA islands transform into secondary martensite upon cooling. The M2/RA islands consist of the M2 core surrounded by the RA shell. The bright contrast of the boundaries of M2/RA islands with the M1 and BF constituents supports this statement (Fig. 5a). Inhomogeneous carbon distribution in the blocky-type RA induces the difference in contrast between the shell and core regions (Fig. 5a).

The areas of untransformed austenite with C < 1 wt% and C < 1.4 wt% may be replaced by BF and the M2 constituents during partitioning and cooling, respectively. Carbon in martensite could diffuse to RA within 1 s of isothermal holding [7], but the whole volume of blocky RA could not consume equilibrium carbon mass during 20 s partitioning

(Table 2). Thin inclusions of BF with irregular shape within coarse M2/RA islands are observed (Fig. 5a). These plates of BF may play a role as a diffusion path for carbon enrichment of RA during further partitioning.

The distribution of carbides in the M1 constituent is inhomogeneous. A major portion of primary martensite areas contains low densities of carbides, and dense carbide precipitations were observed in some areas only (Fig. 5a). Density of carbides is strongly dependent on martensite orientation. BF appeared as a carbide-free structural constituent with an irregular shape. Therefore, processes of carbon partitioning between primary martensite and untransformed austenite, bainite transformation, and precipitation of carbides occur concurrently.

At t_p~60 s, the contrast between primary martensite and the M2/RA islands becomes distinctly distinguished, that is indicates for strong carbon partitioning between these constituents (Fig. 5b). The $\overline{X}_\gamma$ value makes feasible the carbon enrichment of the core regions of the M2/RA with a highest dimension ≤700 nm (Fig. 5b, Table 2). Carbide-free BF subunits exhibiting a plate-like shape [22] are observed within the majority of coarse M2/RA islands located at PAG boundaries (Fig. 5b). These bainitic subunits have a thickness of <200 nm. A minor portion of the M2/RA islands is subdivided by coarse carbide-free BF into thin lamellas with an average thickness of <200 nm (Fig. 5b). In addition, sheaves of BF with an average thickness of ~500 nm alternate with the M2/RA islands exhibiting a plate-like shape and nearly the same thickness (Fig. 5b). The number density and volume fraction of carbides in the M1 constituent increase, and the interparticle spacing decreases with increasing partitioning time from 20 to 60 s (Figs. 5 and 6c,
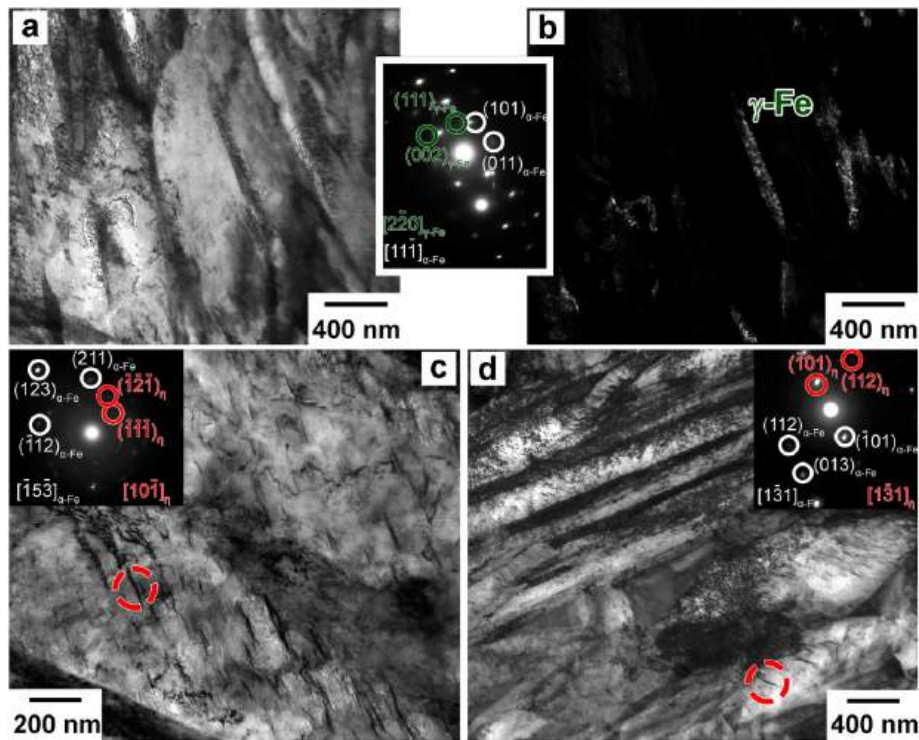
Fig. 6. Bright field (a) and dark field (b) TEM image showing film-like RA and transition carbides after partitioning for 60 s (c) and 1000 s (d).

Table 2). Identification of carbides by TEM technique revealed only transition η-Fe$_2$C carbides (Fig. 6c and d, EDS analysis of carbon replicas was not presented here). Therefore, it is obvious that all carbides observed at SEM micrographs (Fig. 5) are transition η-Fe$_2$C ones. Transition carbides exhibit a plate-like shape and locate in lath along two mutually perpendicular planes of ferrite producing a 2D array (Fig. 6c and d). At $t_p > 60$ s, the volume fraction of carbides remains nearly unchanged (Fig. 6c and d, Table 2). Therefore, a major portion of transition carbides with a plate-like shape precipitated upon partitioning with $t_p \sim 60$ s. Mass balance analysis (Eq. (12), Table 2) showed that the average carbon concentration in transition carbides is 16 at.%. It is worth noting that η-Fe$_2$C carbides could precipitate with the lowest non-stoichiometric carbon concentration of 13 at.% [25,62,63]. Further partitioning leads to the gradual transformation of non-stoichiometric transition carbides to stoichiometric ones due to carbon enrichment up to 33 at.%C that is the stoichiometric carbon concentration of η-Fe$_2$C carbides [41,63]. At $t_p \sim 500$ s, mass balance analysis (Eq. (12), Table 2) showed that the carbon atomic concentration in transition carbides attains 31 at.%. Therefore, the precipitation of non-stoichiometric carbides could not compensate the volume expansion attributed to the formation of bainitic subunits (Figs. 2 and 3). The transition from the non-stoichiometric chemical composition of η-Fe$_2$C carbides to the stoichiometric one is accompanied by the transformation of austenite to bainite with increasing t_p (Table 3, Fig. 3). The highest number density of transition carbides is achieved after $t_p \sim 1000$ s (Table 3). A weak

coarsening of the transition carbides occurs that leads to a decrease in its aspect ratio from 15.0 after $t_p \sim 60$ s to 11.5 after $t_p \sim 1000$ s (Table 3).

The subdivision of blocky RA by bainitic lamellas is the main process of microstructural evolution taking place with increasing t_p from 60 to 500 s (Fig. 5c). At $t_p \sim 300$ s, the majority of the M2/RA islands exhibits an irregular shape. These islands locate at the block and packet boundaries (Fig. 5c). The formation of BF occurs within the M2/RA islands and at M1/RA interfaces. In the first case, the bainitic plates are surrounded by the M2/RA shell, and the whole M2/RA islands are subdivided by BF plates into chains of small islands with an irregular shape (Fig. 5c). These small islands may be connected by a film-like RA (Fig. 5c). In the second case, the composite M2/RA/bainite areas with a lenticular shape appear. Increasing partitioning time from 60 to 300 and 500 s decreases the thickness and volume fraction of the M2/RA islands (Fig. 5b–d, Table 2). Upon $t_p \sim 500$ s the majority of the M2/RA islands become thin, and the thickness of RA lamellas is ≤ 200 nm (Fig. 5d). Thickness of the M2/RA islands decreases with increasing t_p from 60 to 500 s. This fact is attributed to carbon enrichment of blocky RA due to the shortening diffusion path (Table 2). At $t_p \sim 500$ s, volume fractions of film-like and blocky RA are nearly the same (Fig. 5d). The main feature of this partitioned structure is a high volume fraction of carbide-free BF (Fig. 5d).

Increasing the partitioning time from 500 to 1000 s leads to an increase in the thickness of the M2/RA islands and a decrease in the thickness of bainitic plates located within these islands ≤ 200 nm

Table 3
Effect of partitioning time on volume fraction of RA calculated by the EBSD technique, particle density and dimensions of transition carbides calculated by the TEM technique, volume fraction of η-carbides obtained from SEM observations, the ρ_{KAM} values of martensite (BCC) and RA (FCC).

Partitioning time, s	Volume fraction of RA, %	length/width of η-carbide, nm	Distance between η-carbides, nm	Particle density (η-carbides), $\times 10^{12}$ m^{-2}	Volume fraction of η-carbides, %	BCC ρ_{KAM}, $\times 10^{15}$ m^{-2} $^\circ$	FCC ρ_{KAM}, $\times 10^{15}$ m^{-2} $^\circ$
20	14	72/6	96.0	9.08	3.5	0.94	0.77
60	36	74/5	58.6	19.3	4.6	0.8	0.82
300	34	–	–	–	4.8	0.87	0.84
500	4	85/7	58.1	19.7	4.8	0.94	0.7
1000	9.4	92/8	47.2	22.8	4.9	0.99	0.83

(Fig. 5e, Table 2). In addition, relatively coarse bainitic areas with irregular shapes are observed within the M2/RA islands (Fig. 5e). The carbide-free BF locates within these islands or between them and the areas of primary martensite (Fig. 5e). The film-like RA is rarely observed. The growth of untransformed austenite crystallites with nearly round shapes took place. At $t_p \geq 500$, the diffusion distance is sufficient for complete homogenization of austenite core regions during partitioning (Table 2). However, secondary martensite appears due to the displacive transformation occurring in carbon depleted areas of untransformed austenite.

TEM observations (Fig. 6a and b) showed that the thickness of film-like RA is 160 ± 31 nm and no significant effect of partitioning time on this parameter was found. The feature of the present Q&P steel is the small spacing between high-angle boundaries in lath martensite structure, d_{HAB} (Table 4). It is worth noting that the d_{HAB} value and the lath thickness, d_l, of this steel processed by Q&P and water quenching followed by tempering at 400 °C [44] are nearly the same. The effect of partitioning on the d_{HAB} and d_l values is insignificant (Table 4), despite the appearance of coarse martensite/BF plates after 60, 300, and 1000 s partitioning (Fig. 7). There is no correlation between the portions of the M1 and M2 constituents, BF (Table 1) and d_{HAB}/d_l values (Table 4). The high dislocation densities were revealed by TEM observations (ρ_{TEM}) (Fig. 6) and the KAM analysis (ρ_{KAM}) [8]. The densities of lattice dislocations $\rho_{TEM}\sim 2 \times 10^{15}$ m^{-2} in RA and secondary martensite were essentially the same [8]. The ρ_{TEM} value is higher than ρ_{KAM} one by a factor of $\sim$2 (Table 3), that is indicative for a high number of lattice dislocations introduced to accommodate shape deformation of the martensitic transformation [18,22,41].

In the present study, the EBSD technique strongly overestimates the volume fraction of RA at partitioning times ranging from 20 to 300 s (Fig. 4a, Table 3). It is known [64] that EBSD techniques usually underestimates the volume fraction of RA due to the fact that the detection limit of this technique does not allow detecting film-like/plates of RA or platelets of martensite/BF with thickness $\leq$200 nm correctly. These films can be erased during the EBSD data by clean-up procedure [64]. Therefore, only the blocky RA as a unit is usually taken into account for the calculation of the RA volume fraction. In contrast, X-ray and magnetic induction techniques provide the calculation of whole RA volume and these data are independent on RA morphology [64]. At $t_p \geq 500$ s, EBSD, X-ray, and magnetic induction techniques provide essentially the same values of RA volume fraction (Fig. 4a, Table 3).

At $t_p\sim$20 s, the blocky RA locates at the packet and PAG boundaries and exhibits an essentially round shape (Fig. 7a). Upon $t_p\sim$60 s, the dimension of RA blocks (Table 2) and volume fraction of this phase increase (Table 3). The blocky RA exhibits irregular shape and locates at the packet and block boundaries comprising semi-continuous chains (Fig. 7b). At $t_p\sim$300 s, RA shows the highest dimension (Table 2). Continuous chains of RA blocks with rectangular and/or irregular shapes are observed at the block boundaries (Fig. 7c). Upon 500 s the RA dimensions (Table 2) and volume fraction (Table 3) decrease sharply. Fine RA blocks with round shapes are observed at the boundaries of PAGs and packets (Fig. 7d). At $t_p\sim$1000 s, the size and volume fraction of RA increase (Tables 2 and 3). Semi-continuous chains of RA appear on the PAG boundaries (Fig. 7e).

3.3. Mechanical properties

Engineering stress-strain curves, the effect of strain on strain hardening rate, $d\sigma/d\varepsilon$, are shown in Fig. 8 after different partitioning regimes, and the effect of partitioning on the YS, UTS, elongation-to-failure, and the PSE is summarized in Table 5. All σ-ε curves exhibit continuous yielding [57,65] followed by the work-hardening stage up to the onset of necking. Upon 60 s the stress-strain curves exhibit jerky flow associated with the Portevin-Le Chatelier (PLC) effect [57,65]. Partitioning increases the YS slightly and decreases UTS (Table 5). However, high PSE>24.5 GPa×% is observed after all partitioning times. The elongation-to-failure, uniform elongation, and the PSE increase with increasing the partitioning time from 20 up to 300 s and the PSE attains a very high value of 35.3 GPa×% (Table 5). Highest PSE and ductility attain if the highest portion of RA transforms to strain-induced martensite (Fig. 4b) and blocky RA is subdivided by plates of BF. The effect of morphology and carbon concentration of RA on the PSE in the present steel is considered in the companion article [66] in detail. At $t_p \leq 300$ s, high elongation-to-failure and superior PSE values are attributed to the transformation of the major portion of RA to strain-induced martensite during tension [66]. It was assumed [16] that the transformation of RA to strain-induced martensite during tension inhibits necking that increases elongation-to-failure.

At $t_p \geq 500$ s, the susceptibility of the steel to necking is low, and the Q&P steel exhibits decreased values of the elongation-to-failure and the PSE. Upon 1000 s the fracture occurs without necking. The values of elongation-to-failure and uniform elongation become essentially the same (Table 5). The elongation-to-failure and the PSE decrease due to premature fracture without necking. It is worth noting that present results show that necking correlates with the occurrence of the RA→strain-induced martensite transformation during tension [66]. If RA becomes less feasible for transformation to strain-induced martensite, the onset of premature fracture occurs before necking [66]. However, the steel exhibits superior values of ductility and the PSE>2.5 × 10^4 MPa × % after $t_p \geq 500$ s despite limited formation of strain-induced martensite during tension (Fig. 4). This phenomenon could be associated with intense twinning within RA [66]. Intense strain hardening and ductility are provided by twinning induced plasticity (TWIP) [67]. Thus, at $t_p > 300$ s, the enrichment of RA by carbon during partitioning hinders the transformation of RA to strain-induced martensite and promotes twining [66,67].

At t_p ranging from 20 to 300 s, the onset of the Considère condition [57,65]:

$$\frac{d\sigma}{d\varepsilon} = \sigma \tag{13}$$

correlates with the transition from stable plastic flow to unstable one (Fig. 8b-the strain-strain hardening curve for $t_p\sim$300 s is not shown here). Increasing the partitioning time from 20 to 60 s shifts the onset of the Considère condition and necking to higher strains. The strain for the onset of the Considère condition remains nearly unchanged for the partitioning time ranging from 60 to 500 s (Fig. 8b). At $t_p \geq 500$ s, the onset of fracture occurs at the stage of stable plastic flow and is revealed as a sudden drop. Therefore, the effect of partitioning time on necking is attributed to the transition from transformation of RA into strain-induced martensite to intense twinning in this phase during tension due to progressive carbon enrichment of RA [66].

3.4. Phase transformations during partitioning

Inspection of experimental results shows that the 0.44 wt%C steel exhibits unique phase transformations during partitioning due to the large volume fraction of untransformed blocky austenite. Several processes occur concurrently and/or sequentially in blocky-type austenite (Figs. 3, 9 and 10).
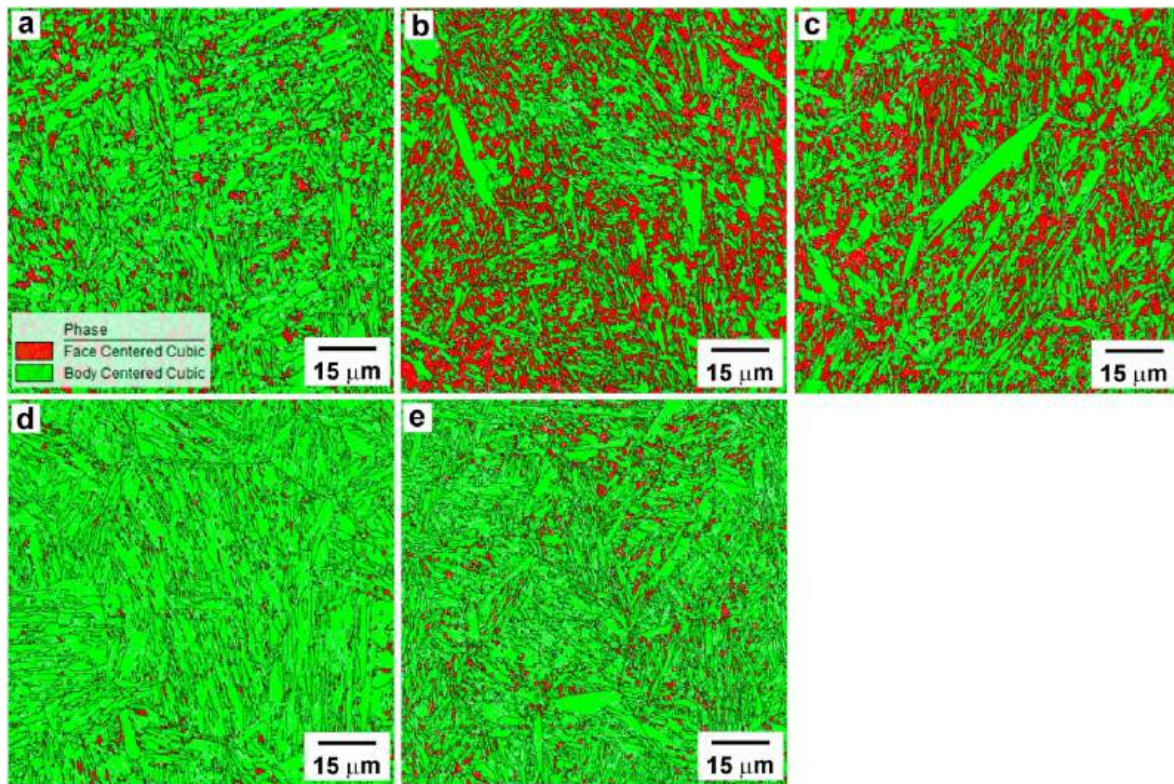
Table 4
Effect of partitioning time on average spacing between high-angle boundaries, d_{HAB}, lath thickness, d_l.

Partitioning time, s	d_{HAB}, µm	d_l, nm
20	0.77 ± 0.15	277 ± 40
60	0.72 ± 0.12	293 ± 45
300	0.78 ± 0.15	–
500	0.88 ± 0.2	245 ± 42
1000	0.73 ± 0.15	261 ± 40

Fig. 7. EBSD analysis of the Fe-0.44C steel after partitioning during 20 s (a), 60 s (b), 300 s (c), 500 s (d), and 1000 s (e), RA is emphasized by the red color. The low- and high-angle boundaries with misorientations of $2° \leq \theta < 15°$ and $\geq 15°$ depicted by white and black lines, respectively. (For interpretation of the references to color in this figure legend, the reader is referred to the Web version of this article.)
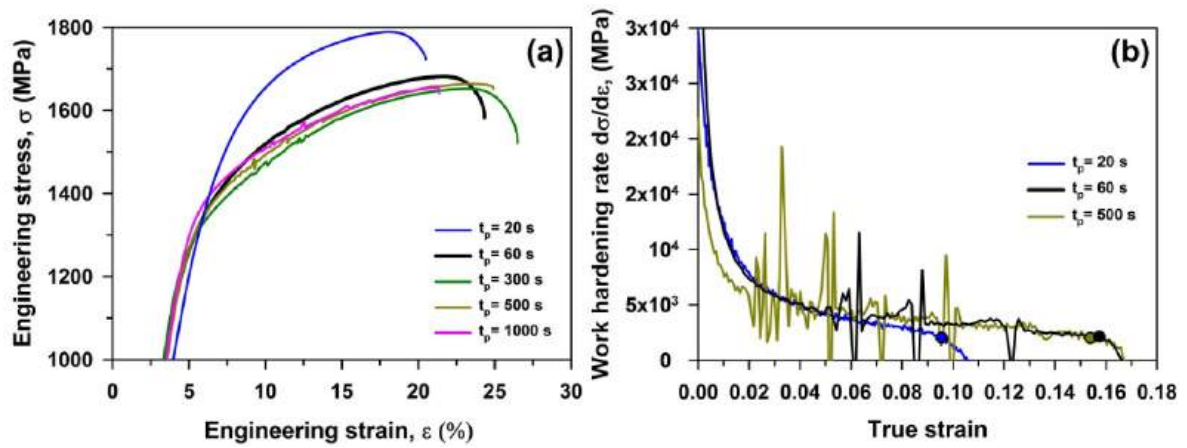

Fig. 8. Typical engineering stress–strain curves (a) and strain hardening vs. strain curves with circles showing the onset of the Considère condition (Eq. (13)) (b).

Table 5
Mechanical properties of the Fe-0.44%C steel after partitioning at different times.

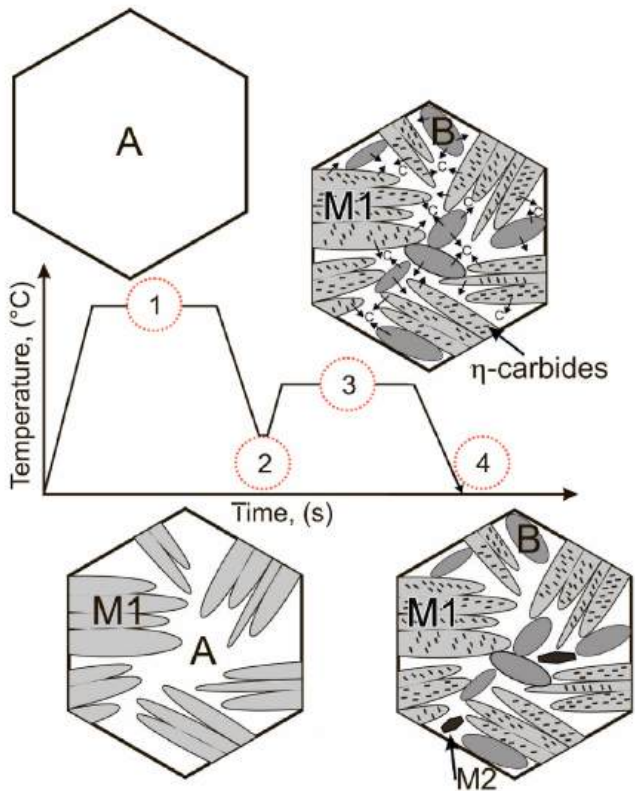| Partitioning time, s	Hardness, HRC	YS, MPa	UTS, MPa	Elongation-to- failure, %	Uniform elongation, %	PSE, MPa·%
20	49 ± 2	1110	1790	13.7	10.2	24 523
60	48 ± 2	1120	1680	18.9	17.3	31 752
300	48 ± 2	1150	1650	21.4	17.5	35 310
500	50 ± 2	1170	1660	19.1	17.1	31 706
1000	49 ± 2	1210	1650	15.6	14.7	25 740

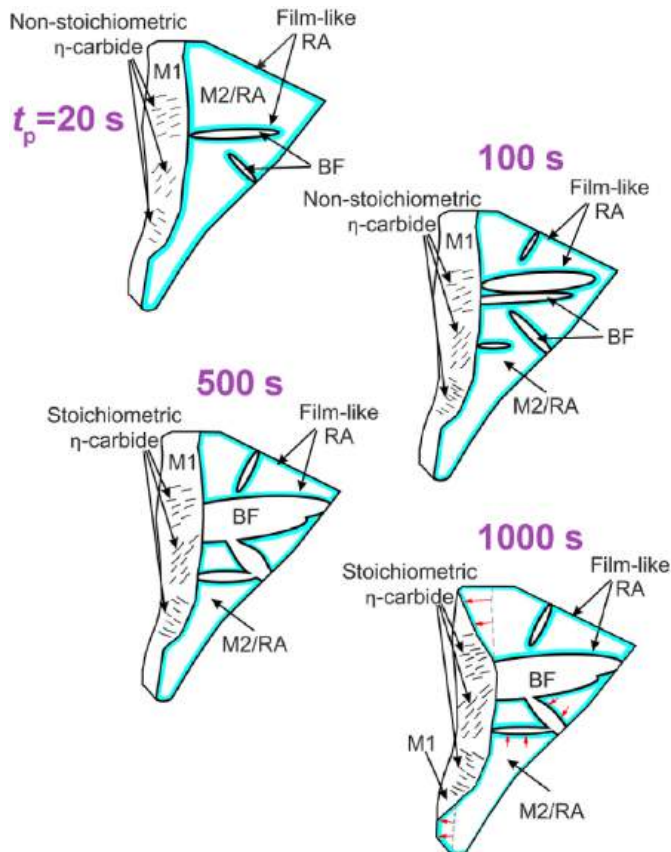**Fig. 9.** Schematic illustration of the microstructural evolution during Q&P.

Fig. 10. Effect of partitioning time on the microstructure.

(i) Carbon partitioning from martensite to RA;
(ii) Bainitic transformation: (iia) diffusionless fast growth of sub-units/frontal growth and (iib) slow growth of sheaves controlled by carbon diffusion/edgewise growth;
(iii) Precipitation of transition η–Fe$_2$C carbides in the martensitic matrix and its carbon enrichment up to stoichiometric composition;
(iv) Paraequilibrium transformation of the M1/BF constituents to austenite controlled by carbon diffusion.

The carbon partitioning from martensite to film-like RA occurs at a high rate due to the small thickness of this phase. No remarkable effect of partitioning time on a dispersion of this phase was found. As a result, we will pay attention to phase transformations occurring in blocky type of RA.

The kinetic of bainitic transformation could be described by the Kolmogorov–Johnson–Mehl–Avrami (KJMA) equation at small partitioning times [14,53]:

$$f^{BF} = 1 - exp\left(-(kt)^n\right), \tag{14}$$

where n is the Avrami exponent and k is the transformation rate constant. The obtained n and k values are shown in Fig. 2a''-c''. Eq. (14) with k = 0.09364 and n = 0.74933 describes the dilatation curve with high and satisfactory accuracy up to 100 s and in the t_p interval 100–250 s, respectively (Fig. 2a''-c''). Analysis of experimental data showed that Eq. (14) describes kinetics of the diffusionless growth of bainitic subunits occurring at a high rate and could be used for interpretation of the dilatation curve at the initial stage of bainitic transformation when the growing BF inherits the composition of untransformed austenite [22,41] (Fig. 3). It is known [9,22,35,41,53,55] that at initial stages, the diffusionless bainitic transformation occurs through the growth of subunits without significant carbon redistribution from BF to untransformed austenite taking into account that the rate of BF/γ interface migration is lower than the rate of carbon enrichment of the layer in untransformed austenite by a factor of ~220. The subunits adopt the morphology of a plate [22]. Carbon enrichment of RA slows down this phase transformation. At higher partitioning times, several processes contribute to net dilatation, and Eq. (14) could not provide an appropriate description of experimental data.

At t_p~100 s, the growth of subunits ends (Figs. 3 and 10). Further partitioning provides additional carbon enrichment of RA up to 1.4 wt% C and bainitic transformation may occur through sheaf growth controlled by carbon redistribution [9,22,35,41,55]. This transformation occurs with a low rate [22.41]. The sheaves of BF are carbon depleted and their formation produces insignificant net dilatation. The main feature of bainitic transformation in this Si-rich steel is lacking or insignificant precipitation of transition carbides in BF [1,3,22,55]. At t_p ≤ 500 s, the chains of bainitic subunits play a role of diffusion path for carbon redistribution from martensite to untransformed austenite [12], in addition to one from BF to the austenite directly (Fig. 10).

Bainitic transformation in blocky untransformed austenite occurs in four sequential steps [9,22,41]. Nucleation of BF taking place at martensite/austenite interfaces is followed by fast growth of bainitic plates in longitudinal direction at right angle to the interface during the partitioning step (Fig. 10) [9,22,44,53,55]. The growing plates are fine and exhibit a lenticular shape. Their thickness is usually ≤300 nm [22,41]. At t_p ≤ 60s, these plates subdivide whole areas of blocky RA into plates with irregular shapes (Fig. 5a–c). These lenticular subunits of BF could not be resolved within blocky RA by the EBSD technique used in the present study. As a result, the bainite/RA islands are interpreted as whole RA islands after a clean-up procedure that leads to the overestimation of RA volume fraction by the EBSD technique upon t_p ranging from 60 to 300 s (Fig. 4, Table 3). Next, individual platelets of BF compose sheaves [9,22,41]. Their growth occurs in a parallel direction to the martensite/austenite interfaces, that leads to the irregular shape

of the bainite/M2/RA islands (Fig. 10).

The diffusion controlled edgewise growth rate of bainite could be calculated by the well-known Zener-Hillert equation [9,36] as:

$$V_{max} = \frac{(X^\gamma - X_0)^2}{(X_0 - X^\alpha)} \frac{DRT}{8\sigma V_m} \tag{15}$$

where V_{max} is the highest growth rate, X^γ and X^α are the equilibrium mole fractions of C in austenite and ferrite, respectively, calculated from Thermo-Calc at the ferrite/austenite interface, $X_0 = 0.019738$ is the overall mole fraction of carbon in the steel, $\sigma = 0.2$ J/m^2 is the interfacial energy per unit area, and $V_m = \left(1 + 3.6 \bullet 10^{-5}(T - 298)\right)7.09 \bullet 10^{-6}$ m^3/mol is the molar volume of ferrite. The highest edgewise growth rate was calculated to be 0.103 μm/s. It is obvious that the average growth rate is small [35]. However, this growth rate could provide the formation of thick plates of bainitic ferrite within untransformed austenite and the occurrence of bainitic transformation through the diffusion-controlled mechanism at $t_p > 100$ s. Edgewise growth of sheaves leads to the fact that untransformed austenite retains between the platelets and sheaves in the form of thin films [9,41]. These films could not be resolved by the EBSD technique, and the bainite/RA islands are interpreted as whole ferrite islands that leads to the underestimation of the RA volume fraction by the EBSD technique at $t_p{\sim}500$ s (Fig. 4, Table 3). Thus, the unusual discrepancy between the volume fraction of RA calculated by the EBSD technique and X-ray/magnetic saturation measurements in the present study is attributed to the transition from the displacive mechanism of bainitic transformation at $t_p \leq 100$ s to the diffusion-controlled mechanism at $t_p \geq 300$ s.

Heterogeneous nucleation of the transition carbides on dislocations [25,46] occurs at a high rate during partitioning. However, the transition from a non-stoichiometric composition of ~13 at.%C to a stoichiometric composition of 33 at.%C requires a long-range diffusion flux of carbon and occurs up to $t_p{\sim}1000$ s [25,63]. This process results in carbon depletion from the matrix of primary martensite down to the thermodynamically equilibrium value in ferrite [24,33,41] that promotes the paraequilibrium transformation of M1, BF, to RA controlled by carbon diffusion due to the appearance of a large difference in Gibbs energies between the constituents with bcc and fcc lattices at $t_p > 500$ s (Figs. 3 and 10). Thus, the carbon enrichment of transition η-Fe$_2$C carbides promotes the growth of untransformed austenite through the paraequilibrium transformation mechanism at $t_p > 500$ s. Newly formed areas of austenite are characterized by a relatively low C content and susceptible to transformation to the M2 constituent during final cooling. Therefore, the inhomogeneous distribution of carbon concentrations over the blocks of austenite associated with a low diffusion rate causes the formation of secondary martensite at all partitioning times.

4. Conclusions

The Fe-0.44%C-1.8%Si-1.3%Mn-0.82%Cr-0.28%Mo steel was processed by Q&P, including quenching at 200 °C for 15 s followed by partitioning at 400 °C with a time range of 20 to 1000 s. The main conclusions are following.

1) The steel exhibits the YS ≥ 1100 MPa and the PSE≥24.5 GPa·% after all partitioning times, with a superior combination of the YS = 1150 MPa and the PSE≥35.3 GPa·% after $t_p{\sim}300$ s. The high PSE values are associated with the transformation of RA into strain-induced martensite during tension. The carbon enrichment of RA hinders this transformation. However, the PSE remains high enough due to the occurrence of extensive twinning in RA during tension.
2) The volume fraction of RA increases from ~12 to ~18 % with increasing the partitioning time from 20 to 60 s and decreases to ~7.5 % at $t_p{\sim}500$ s. Further partitioning up to 1000 s increases the volume fraction of RA to ~10 %. The carbon content in RA is ~1.4 wt % in the partitioning time interval 20–500 s and increases up to 1.6

wt% at $t_p{\sim}1000$ s. The unusual effect of partitioning time on microstructure and phase composition is attributed to features of phase transformations in blocky type austenite. At $t_p \leq 100$ s, the carbon partitioning from martensite to untransformed austenite and bainitic transformation occur concurrently. The carbon enrichment of austenite up to 1 wt%C ceases diffusionless bainitic transformation. In the partitioning time interval 100–500 s the bainitic transformation occurs through the edgewise sheaf growth controlled by carbon partitioning. At $t_p > 500$ s, the paraequilibrium transformation of the M1, BF to austenite controlled by carbon diffusion leads to the growth of RA blocks. Film-like RA is enriched by carbon after $t_p {\sim}20$ s and remains virtually unchanged up to $t_p {\sim}1000$ s.
3) Precipitation of the transition η-Fe$_2$C carbides takes place after 20 s partitioning. At $t_p {\sim}60$ s, the volume fraction of these carbides attains 4.6 % and insignificantly increases upon further partitioning. The number density and interparticle spacing of carbides increase and decrease continuously with increasing the partitioning time, respectively. Analysis of carbon mass balance showed that the carbon enrichment of the transition carbides occurs at $t_p > 60$ s that leads to the transformation of non-stoichiometric η-Fe$_2$C carbides into stoichiometric ones during partitioning. This process strongly affects the relationship between the volume fraction of martensite and untransformed austenite and the carbon content in RA.
4) The effect of partitioning time on the volume fraction of secondary martensite is insignificant due to the heterogeneous carbon distribution in blocky-type RA.

CRediT authorship contribution statement

R. Mishnev: Writing – review & editing, Visualization, Validation, Methodology, Investigation, Formal analysis, Data curation, Conceptualization. **Yu. Borisova:** Writing – review & editing, Visualization, Validation, Methodology, Investigation, Formal analysis, Data curation. **T. Kniaziuk:** Investigation. **R. Kaibyshev:** Writing – review & editing, Writing – original draft, Supervision, Project administration, Funding acquisition, Conceptualization.

Declaration of competing interest

The authors declare that they have no known competing financial interests or personal relationships that could have appeared to influence the work reported in this paper.

Data availability

Data will be made available on request.

Acknowledgments

References

[1] N. Fonstein, Advanced High Strength Sheet Steels, Springer International Publishing, Cham, 2015, https://doi.org/10.1007/978-3-319-19165-2.
[2] J. Speer, D.K. Matlock, B.C. De Cooman, J.G. Schroth, Carbon partitioning into austenite after martensite transformation, Acta Mater. 51 (2003) 2611–2622, https://doi.org/10.1016/S1359-6454(03)00059-4.
[3] J. Zhao, Z. Jiang, Thermomechanical processing of advanced high strength steels, Prog. Mater. Sci. 94 (2018) 174–242, https://doi.org/10.1016/j.pmatsci.2018.01.006.

[4] B. An, C. Zhang, G. Gao, X. Gui, Z. Tan, R.D.K. Misra, Z. Yang, Experimental and theoretical analysis of multiphase microstructure in a newly designed MnSiCrC quenched and partitioned steel to promote bainitic transformation: the significant impact on mechanical properties, Mater. Sci. Eng. 757 (2019) 117–123, https://doi.org/10.1016/j.msea.2019.04.099.

[5] E.J. Seo, L. Cho, Y. Estrin, B.C. De Cooman, Microstructure-mechanical properties relationships for quenching and partitioning (Q&P) processed steel, Acta Mater. 113 (2016) 124–139, https://doi.org/10.1016/j.actamat.2016.04.048.

[6] D.T. Pierce, D.R. Coughlin, D.L. Williamson, K.D. Clarke, A.J. Clarke, J.G. Speer, E. De Moor, Characterization of transition carbides in quench and partitioned steel microstructures by Mössbauer spectroscopy and complementary techniques, Acta Mater. 90 (2015) 417–430, https://doi.org/10.1016/j.actamat.2015.01.024.

[7] F. HajyAkbary, J. Sietsma, G. Miyamoto, T. Furuhara, M.J. Santo, Interaction of carbon partitioning, carbide precipitation and bainite formation during the Q&P process in a low C steel, Acta Mater. 104 (2016) 72–83, https://doi.org/10.1016/j.actamat.2015.11.032.

[8] R. Mishnev, Y. Borisova, S. Gaidar, T. Kniaziuk, O. Vagina, R. Kaibyshev, Q&P response of a medium carbon low alloy steel, Metals 13 (2023) 689, https://doi.org/10.3390/met13040689.

[9] Z. Dai, H. Chen, R. Ding, Q. Lu, C. Zhang, Z. Yang, S. Zwaag, Fundamentals and application of solid-state phase transformations for advanced high strength steels containing metastable retained austenite, Mater. Sci. Eng. R 143 (2021) 100590, https://doi.org/10.1016/j.mser.2020.100590.

[10] Y. Takahama, M.J. Santofimia, M.G. Mecozzi, L. Zhao, J. Sietsma, Phase field simulation of the carbon redistribution during the quenching and partitioning process in a low-carbon steel, Acta Mater. 60 (2012) 2916–2926. https://doi:10.1016/j.actamat.2012.01.055.

[11] E. Tkachev, S. Borisov, Y. Borisova, T. Kniaziuk, S. Gaidar, R. Kaibyshev, Strength–toughness of a low-alloy 0.25C steel treated by Q&P processing, Materials 16 (2023) 3851, https://doi.org/10.3390/ma16103851.

[12] V.I. Zurnadzhy, V.G. Efremenko, K.M. Wu, I. Petryshynets, K. Shimizu, A.M. Zusin, M.N. Brykov, V.A. Andilakhai, Tailoring strength/ductility combination in 2.5 wt% Si-alloyed middle carbon steel produced by the two-step Q-P treatment with a prolonged partitioning stage, Mater. Sci. Eng. 791 (2020) 139721, https://doi.org/10.1016/j.msea.2020.139721.

[13] A. Arlazarov, M. Ollat, J.P. Masse, M. Bouzat, Influence of partitioning on mechanical behavior of Q&P steels, Mater. Sci. Eng. 661 (2016) 79–86, https://doi.org/10.1016/j.msea.2016.02.071.

[14] E. Tkachev, S. Borisov, Yu Borisova, T. Kniaziuk, A. Belyakov, R. Kaibyshev, Austenite stabilization and precipitation of carbides during quenching and partitioning (Q&P) of low-alloyed Si–Mn steels with different carbon content, Mater. Sci. Eng. 895 (2024) 146212, https://doi.org/10.1016/j.msea.2024.146212.

[15] D. Yang, Z. Xiong, The dependence of fracture resistance on the size and distribution of blocky retained austenite-martensite constituents, Metall. Mater. Trans. 51 (2020) 2072–2083, https://doi.org/10.1007/s11661-020-05698-0.

[16] M. Soleimani, A. Kalhor, H. Mirzadeh, Transformation-induced plasticity (TRIP) in advanced steels, A review, Materials Science and Engineering A 795 (2020) 140023, https://doi.org/10.1016/j.msea.2020.140023.

[17] X.C. Xiong, B. Chen, M.X. Huang, J.F. Wang, L. Wang, The effect of morphology on the stability of retained austenite in a quenched and partitioned steel, Scripta Mater. 68 (2013) 321–324, https://doi.org/10.1016/j.scriptamat.2012.11.003.

[18] N. Nakada, Y. Ishibashi, T. Tsuchiyama, S. Takaki, Self-stabilization of untransformed austenite by hydrostatic pressure via martensitic transformation, Acta Mater. 110 (2016) 95–102, https://doi.org/10.1016/j.actamat.2016.03.048.

[19] J. Chiang, J.D. Boyd, A.K. Pilkey, Effect of microstructure on retained austenite stability and tensile behaviour in an aluminum-alloyed TRIP steel, Mater. Sci. Eng. 638 (2015) 132–142, https://doi.org/10.1016/j.msea.2015.03.069.

[20] I.B. Timokhina, P.D. Hodgson, E.V. Pereloma, Effect of microstructure on the stability of retained austenite in transformation-induced-plasticity steels, Metall. Mater. Trans. 35 (2004) 2331–2341, https://doi.org/10.1007/s11661-006-0213-9.

[21] S. Ebner, R. Schnitzer, E. Maawad, C. Suppan, C. Hofer, Influence of partitioning parameters on the mechanical stability of austenite in a Q&P steel: a comparative in-situ study, Materialia 15 (2021) 101033, https://doi.org/10.1016/j.mtla.2021.101033.

[22] H.K.D.H. Bhadeshia, Bainite in Steels. Transformation, Microstructure and Properties, 2st ed, IOM Communications Ltd., London, UK, 2001.

[23] K. Zhang, P. Liu, W. Li, Zh Guo, Y. Rong, Ultrahigh strength-ductility steel treated by a novel quenching–partitioning–tempering process, Mater. Sci. Eng. 619 (2014) 205–211, https://doi.org/10.1016/j.msea.2014.09.100.

[24] X.X. Dong, Y.F. Shen, N. Jia, Y.T. Zhu, Improving mechanical properties and retained-austenite stability of a medium carbon Q&P steel by adjusting phase ratio, Mater. Sci. Eng. 833 (2022) 142580, https://doi.org/10.1016/j.msea.2021.142580.

[25] D. Yuzbekova, V. Dudko, T. Kniaziuk, R. Kaibyshev, Tempering behavior of an ultra-high-strength steel with 1.6 wt % Si at low to medium temperatures, Mater. Sci. Eng. 896 (2024) 146264, https://doi.org/10.1016/j.msea.2024.146264.

[26] F. Niessen, T. Nyyssonen, A.A. Gazder, R. Hielscher, Parent grain reconstruction from partially or fully transformed microstructures in MTEX, J. Appl. Crystallogr. 55 (2022) 180–194, https://doi.org/10.1107/S1600576721011560.

[27] M. Calcagnotto, D. Ponge, E. Demir, D. Raabe, Orientation gradients and geometrically necessary dislocations in ultrafine grained dual-phase steels studied by 2D and 3D EBSD, Mater. Sci. Eng. 527 (2010) 2738–2746, https://doi.org/10.1016/j.msea.2010.01.004.

[28] F. Peng, Y. Xu, X. Gu, Y. Wang, J. Li, H. Zhan, Microstructure characterization and mechanical behavior analysis in a high strength steel with different proportions of constituent phases, Mater. Sci. Eng. 734 (2018) 398–407, https://doi.org/10.1016/j.msea.2018.08.018.

[29] N. van Dijk, A. Butt, L. Zhao, J. Sietsma, S. Offerman, J. Wright, S. van der Zwaag, Thermal stability of retained austenite in TRIP steels studied by synchrotron X-ray diffraction during cooling, Acta Mater. 53 (2005) 5439–5447, https://doi.org/10.1016/j.actamat.2005.08.017.

[30] R. Ranjan, H. Beladi, P.D. Hodgson, S.B. Singh, The mechanical properties of low alloy TRIP-aided steel: the role of retained austenite, Metall. Mater. Trans. 52 (2021) 4649–4663, https://doi.org/10.1007/s11661-021-06417-z.

[31] J. Hidalgo, R.M. Huizeng, K.O. Findley, M.J. Santofimia, Interplay between metastable phases controls strength and ductility in steels, Mater. Sci. Eng. 745 (2019) 185–194, https://doi.org/10.1016/j.msea.2018.12.096.

[32] S.M.C. van Bohemen, Bainite and martensite start temperature calculated with exponential carbon dependence, Mater. Sci. Technol. 28 (2012) 487–495, https://doi.org/10.1179/1743284711Y.0000000097.

[33] E.J. Seo, L. Cho, J.K. Kim, J. Mola, L. Zhao, B.C. De Cooman, Constituent-specific properties in quenching and partitioning (Q&P) processed steel, Mater. Sci. Eng. 740–741 (2019) 439–444, https://doi.org/10.1016/j.msea.2018.10.082.

[34] H.Y. Li, X.W. Lu, W.J. Li, X.J. Jin, Microstructure and mechanical properties of an ultrahigh-strength 40SiMnNiCr steel during the one-step quenching and partitioning process, Metall. Mater. Trans. 41 (2010) 1284–1300, https://doi.org/10.1007/s11661-010-0184-8.

[35] S. Samanta, P. Biswas, S. Giri, Sh Brat Singh, S. Kundu, Formation of bainite below the MS temperature: kinetics and crystallography, Acta Mater. 105 (2016) 390–403, https://doi.org/10.1016/j.actamat.2015.12.027.

[36] M.J. Santofimia, L. Zhao, R. Petrov, C. Kwakernaak, W.G. Sloof, J. Sietsma, Microstructural development during the quenching and partitioning process in a newly designed low-carbon steel, Acta Mater. 59 (2011) 6059–6068, https://doi.org/10.1016/j.actamat.2011.06.014.

[37] D. Kim, J. Speer, H. Kim, B. De Cooman, Observation of an isothermal transformation during quenching and partitioning processing, Metall. Mater. Trans. 40 (2009) 2048–2060, https://doi.org/10.1007/s11661-009-9891-4.

[38] A. Navarro-Lòpez, J. Sietama, M.J. Santofimia, Effect of prior athermal martensite on the isothermal transformation kinetics below Ms in a low-C high-Si steel, Metall. Mater. Trans. 47 (2016) 1028–1039, https://doi.org/10.1007/s11661-015-3285-6.

[39] O. Madelung, Landolt-Börnstein. Numerical data and functional relationships in science and technology, in: New Series. Group III: 'Crystals and Solid State Physics'. 'Diffusion in Solid Metals and Alloys', vol. 26, Springer-Verlag, Berlin, 1990, pp. 49–268. A.

[40] S. Kim, J. Lee, F. Barlat, M.-G. Lee, Transformation kinetics and density models of quenching and partitioning (Q&P) steels, Acta Mater. 109 (2016) 394–404, https://doi.org/10.1016/j.actamat.2015.11.051.

[41] H.K.D.H, Bhadeshia Theory of Transformation in Steels, CRC Press. Taylor & Francis group, Boca Raton, FL, USA, 2021, pp. 381–417.

[42] M.J. Santofimia, J.G. Speer, A.J. Clarke, L. Zhao, J. Sietsma, Influence of interface mobility on the evolution of austenite–martensite grain assemblies during annealing, Acta Mater. 57 (2009) 4548–4557, https://doi.org/10.1016/j.actamat.2009.06.024.

[43] M.J. Santofimia, L. Zhao, J. Sietsma, Model for the interaction between interface migration and carbon diffusion during annealing of martensite–austenite microstructures in steels, Scripta Mater. 59 (2008) 159–162, https://doi.org/10.1016/j.scriptamat.2008.02.045.

[44] R. Mishnev, Y. Borisova, T. Kniaziuk, S. Gaidar, R. Kaibyshev, Quench and tempered embrittlement of ultra-high-strength steels with transition carbides, Metals 13 (2023) 1399, https://doi.org/10.3390/met13081399.

[45] M.C. Somani, D.A. Porter, L.P. Karjalainen, R.D.K. Misra, On various aspects of decomposition of austenite in a high-silicon steel during quenching and partitioning, Metall. Mater. Trans. 45 (2014) 1247–1257, https://doi.org/10.1007/s11661-013-2053-8.

[46] S. Borisov, Yu Borisova, E. Tkachev, T. Kniaziuk, R. Kaibyshev, Tempering behavior of a Si-rich low-alloy medium carbon steel, Metals 13 (2023) 1403, https://doi.org/10.3390/met13081403.

[47] Hongqing Zheng, Jiazhi Zhang, Xunwei Zuo, Yonghua Rong, Jianfeng Wan, Nailu Chen, Multi-interface migration mechanism induced by carbide precipitation during the quenching-partitioning-tempering process in a high-carbon steel, Int. J. Plast. 175 (2024) 103928, https://doi.org/10.1016/j.ijplas.2024.103928.

[48] Z.B. Dai, R. Ding, Z.G. Yang, C. Zhang, H. Chen, Thermo-kinetic design of retained austenite in advanced high strength steels, Acta Mater. 152 (2018) 288–299.

[49] S. Dhara, S.M.C. van Bohemen, M.J. Santofimia, Isothermal decomposition of austenite in presence of martensite in advanced high strength steels: a review, Mater. Today Commun. 33 (2022) 104567, https://doi.org/10.1016/j.mtcomm.2022.104567.

[50] M.J. Santofimia, L. Zhao, J. Sietsma, Volume change associated to carbon partitioning from Martensite to Austenite, Mater. Sci. Forum 706–709 (2012) 2290–2295. https://doi.org/10.4028/www.scientific.net/MSF.706-709.2290.

[51] Sh Chen, J. Hu, L. Shan, Ch Wang, X. Zhao, Wei Xu, Characteristics of bainitic transformation and its effects on the mechanical properties in quenching and partitioning steels, Mater. Sci. Eng. 803 (2021) 140706, https://doi.org/10.1016/j.msea.2020.140706.

[52] A.M. Ravi, A. Navarro-López, J. Sietsma, M.J. Santofimia, Influence of martensite/austenite interfaces on bainite formation in low-alloy steels below Ms, Acta Mater. 188 (2020) 394–405, https://doi.org/10.1016/j.actamat.2020.02.003.

[53] Y. Wang, Y. Xu, T. Zhang, J. Li, X. Hou, W. Sun, Effects of quenching temperature on bainite transformation, retained austenite and mechanical properties of hot-galvanized Q&P steel, Mater. Sci. Eng. A (2021) 822, https://doi.org/10.1016/j.msea.2021.141643.

[54] F. Peng, Y. Xu, J. Li, X. Gu, X. Wang, Interaction of martensite and bainite transformations and its dependence on quenching temperature in intercritical quenching and partitioning steels, Mater. Des. 181 (2019) 107921, https://doi.org/10.1016/j.matdes.2019.107921.

[55] Y. Toji, H. Matsuda, D. Raabe, Effect of Si on the acceleration of bainite transformation by pre-existing martensite, Acta Mater. 116 (2016) 250–262, https://doi.org/10.1016/j.actamat.2016.06.044.

[56] X.X. Dong, Y.F. Shena, N. Jia, W.Y. Xue, Simultaneous enhancement of strength and ductility in a medium carbon low-alloy steel induced by secondary martensite and Cu-rich particles, Mater. Sci. Eng. 869 (2023) 144791, https://doi.org/10.1016/j.msea.2023.144791.

[57] G. Krauss, Steels: Processing Structure, and Performance, second ed., ASM International, Materials Park, OH, USA, 2005, p. 64.

[58] W. Bleck, X. Guo, Y. Ma, The TRIP effect and its application in cold formable sheet steels, Steel Res. Int. 88 (2017) 1700218, https://doi.org/10.1002/srin.201700218.

[59] K.W. Andrews, Empirical formulae for calculation of some transformation temperatures, Journal of the Iron and Steel Institute 203 (1965) 721–727.

[60] C. Capdevila, F.G. Caballero, C.G. De Andrés, Determination of m$_s$ temperature in steels: a bayesian neural network model, ISIJ Int. 42 (2002) 894–902, https://doi.org/10.2355/isijinternational.42.894.

[61] J.G. Speer, Phase transformations in quenched and partitioned steels in diffusionless transformation, high strength steels, in: E. Pereloma, D.V. Edmonds (Eds.), Modeling and Advanced Analytical Techniques, vol. 2, Woodhead Publishing Ltd, Cambridge, UK, 2012, pp. 247–270.

[62] E. Tkachev, S. Borisov, Y. Borisova, T. Kniaziuk, R. Kaibyshev, Relationships between strength, ductility and fracture toughness in a 0.33C steel after quenching and partitioning (Q&P) treatment, Crystals 13 (2023) 1431, https://doi.org/10.3390/cryst13101431.

[63] A.J. Clarke, J. Klemm-Toole, K.D. Clarke, D.R. Coughlin, D.T. Pierce, V.K. Euser, J. D. Poplawsky, B. Clausen, D. Brown, J. Almer, P.J. Gibbs, D.J. Alexander, R. D. Field, D.L. Williamson, J.G. Speer, G. Krauss, Perspectives on quenching and tempering 4340 steel, Metall. Mater. Trans. 51 (2020) 4984–5005, https://doi.org/10.1007/s11661-020-05972-1.

[64] F. Vercruysse, C. Celada-Casero, B.M. Linke, P. Verleysen, R.H. Petrov, The effect of Nb on the strain rate and temperature dependent behaviour of quenching & partitioning steels, Mater. Sci. Eng. 800 (2021) 140293, https://doi.org/10.1016/j.msea.2020.140293.

[65] D. Yuzbekova, A. Mogucheva, D. Zhemchuzhnikova, T. Lebedkina, M. Lebyodkin, R. Kaibyshev, Effect of microstructure on continuous propagation of the Portevin–Le Chatelier deformation bands, Int. J. Plast. 96 (2017) 210–226, https://doi.org/10.1016/j.ijplas.2017.05.004.

[66] S. Borisov, Yu Borisova, E. Tkachev, S. Gaidar, R. Kaibyshev, Transformation of Retained Austenite and the Portevin-Le Chatelier Effect in 44CrMn2Si2Mo Steel during Tensile Deformation, Physical Mesomechanics, 2024 (in press).

[67] B.C. De Cooman, Yu Estrin, S.K. Kim, Twinning-induced plasticity (TWIP) steels, Acta Mater. 142 (2018) 283–362, https://doi.org/10.1016/j.actamat.2017.06.046.